energies

MDPI

Article

A Novel Neural Network-Based Droop Control Strategy for Single-Phase Power Converters

Saad Belgana * and Handy Fortin-Blanchette

Department of Electrical Engineering, École de Technologie Supérieure, Montreal, QC H3C 1K3, Canada; handy.fortin-blanchette@etsmtl.ca

* Correspondence: saad.belgana@etsmtl.ca

Abstract: Managing parallel−connected single−phase distributed generators in low−voltage microgrids is challenging due to the volatility of renewable energy sources and fluctuating load demands. Traditional droop control struggles to maintain precise power sharing under dynamic conditions and varying line impedances, leading to inefficiency. This paper presents a novel adaptive droop control strategy integrating artificial neural networks and particle swarm optimization to enhance microgrid performance. Unlike prior methods that optimize artificial neural network parameters, the proposed approach uses particle swarm optimization offline to generate optimal dq−axis voltage references that compensate for line effects and load variations. These serve as training data for the artificial neural network, which adjusts voltage in real time based on line impedance and load variations without online optimization. This decoupling ensures computational efficiency and responsiveness, maintaining voltage and frequency stability during rapid load changes. Addressing dynamic load fluctuations and line impedance mismatches without inter−generator communication enhances reliability and reduces complexity. Simulations demonstrate that the proposed strategy maintains stability, achieves accurate power sharing with errors below 0.5%, and reduces total harmonic distortion, outperforming conventional droop control methods. These findings advance adaptive control in microgrids, supporting seamless renewable energy integration and enhancing the reliability and stability of distributed generation systems.

Keywords: droop control; micro grid; dq control; distributed generation; artificial neural network; particle swarm optimization; single phase inverter; islanding control

Citation: Belgana, S.; Fortin-Blanchette, H. A Novel Neural Network-Based Droop Control Strategy for Single-Phase Power Converters. *Energies* **2024**, *17*, 5825. https://doi.org/10.3390/en17235825

Academic Editors: Antonio T. Alexandridis and Hervé Morel

Received: 28 September 2024
Revised: 6 November 2024
Accepted: 15 November 2024
Published: 21 November 2024

1. Introduction

The global transition towards sustainable energy systems is increasingly driven by the integration of renewable energy sources (RES) and the development of smart grids (SGs). Renewable energies, such as wind and solar power, have gained prominence due to their potential to reduce reliance on fossil fuels and minimize environmental impact. Microgrids (MGs), as key components of SGs, have become essential for managing decentralized energy resources within extensive power networks. By incorporating diverse distributed generation (DG) units, energy storage systems, conversion devices, protection equipment, and loads, MGs offer effective solutions for handling the variability and intermittency associated with RES. Operating in both grid−connected and islanded modes, MGs enhance the reliability and resilience of power systems, especially in regions with high penetration of RES and variable energy availability [1–4].

However, the integration of variable and unpredictable energy sources poses significant challenges to maintaining stable and efficient power distribution [5,6]. A core challenge in MG operation is the dynamic regulation of voltage and frequency for DG units to ensure stable and reliable power supply. Inverters, critical components in DG units, manage the conversion of DC to AC power and are classified as voltage source inverters (VSIs) or current source inverters (CSIs) based on their DC−side storage

elements. Within an MG, DG units and loads can connect or disconnect at any node, necessitating robust control strategies to ensure stable operation during both grid−connected and islanded modes, particularly during network disturbances.

Local control in MGs typically employs the droop control approach, a decentralized method that autonomously adapts to load variations and maintains voltage and frequency stability using only local information. This method effectively manages active and reactive power distribution among DG units without relying on external communication. Traditional droop control methods are well−suited for high−voltage grids with inductive line impedances, where active power (P) and frequency (f), as well as reactive power (Q) and voltage (V), can be decoupled using $(P–f)$ and $(Q–V)$ characteristics. In medium−voltage grids with primarily resistive line impedances, the $(P–V)$ and $(Q–f)$ characteristics are more effective. However, in low−voltage MGs, both inductive and resistive components significantly affect power flow, creating coupling between active and reactive power controls. This mixed impedance environment makes conventional droop control (CDC) methods less effective, causing inaccuracies in power sharing and instability under varying load conditions.

Traditional droop control methods often suffer from several limitations:

- **Inaccurate power sharing due to line impedance variations:** variations in line impedance lead to unequal voltage drops and power−sharing inaccuracies among DG units.
- **Voltage and frequency deviations under load changes:** fixed droop coefficients cannot adapt to sudden fluctuations in load demand, resulting in significant voltage and frequency deviations, compromising power quality and system stability.
- **Limited adaptability to dynamic operating conditions:** traditional methods lack the ability to adjust control parameters in real time, making them ineffective under changing load demands and network configurations.
- **Sensitivity to nonlinear loads and harmonics:** increased Total Harmonic Distortion (THD) occurs due to ineffective handling of nonlinear loads, degrading power quality.
- **Dependence on communication links:** enhancements often require communication between DG units, reducing system reliability and increasing complexity.

To address these limitations, this paper proposes a novel droop control strategy that integrates artificial neural network (ANN) and Particle Swarm Optimization (PSO) to enhance the stability, efficiency, and adaptability of MGs with parallel−connected single−phase DG units. Unlike prior methods where PSO is commonly used to optimize the internal parameters of the ANN, the proposed approach uniquely utilizes PSO during the offline training phase to generate optimal dq−axis voltage reference values that compensate for transmission line effects and load variations. These optimized voltage references serve as training data for the ANN, enabling it to learn the complex relationships between load conditions, line impedances, and the necessary control actions.

By focusing on optimizing control inputs rather than ANN parameters, a dataset of optimal control actions corresponding to different operating scenarios is generated. This data−driven learning enables the ANN to map system measurements to optimal control inputs effectively. During real−time operation, the ANN rapidly computes the required control signals based on real−time measurements, ensuring the necessary responsiveness for MG applications. The ANN−based strategy adjusts control parameters in real time, providing adaptability that fixed−parameter methods lack. This decoupling of the optimization process from real−time operation ensures that the MG control strategy remains responsive and efficient, as the computational demands of PSO do not impact operational performance.

The proposed method specifically targets challenges in MG droop control, such as line impedance mismatches and dynamic load changes. By optimizing control inputs that directly compensate for these variations, improved voltage and frequency stability and accurate power sharing among DG units are achieved. Unlike previous hybrid ANN−PSO approaches that focus on parameter optimization within the controller, this method

addresses droop control optimization in MGs under varying line impedances and load conditions.

By combining these control methods, MG stability is not only maintained but also significantly improved compared with traditional droop control methods. The proposed ANN−based strategy achieves high precision in active and reactive power control by effectively reducing power−sharing errors and enhancing voltage and frequency regulation. This method maintains voltage and frequency stability within tighter bounds, ensuring consistent system performance even under varying load conditions. This directly contributes to the overall objectives of enhancing system performance and improving power quality, as the ANN−based method effectively responds to dynamic changes, mitigates harmonic distortions, and ensures robust and reliable MG operation without the limitations associated with traditional control strategies. These improvements are validated through simulation results presented in the following sections, which demonstrate the effectiveness of the proposed method in achieving superior performance compared with conventional approaches.

The main contributions of this research are as follows:

- **Development of a novel ANN−PSO droop control strategy:** introducing a new approach that integrates ANN and PSO specifically for droop control optimization in MGs.
- **Enhanced MG performance:** improving efficiency, stability, and adaptability in MG operations without relying on communication infrastructure.
- **Addressing practical challenges:** providing solutions for line impedance mismatches, dynamic load changes, and harmonic distortions within a decentralized framework.
- **Practical implementation methodologies:** offering methodologies for implementing advanced control strategies in real−time MG environments.

The rest of the paper is organized as follows: Section 2 reviews the related literature and identifies the research gap; Section 3 discusses conventional droop control methods; Section 4 details the proposed control strategy; Section 5 presents the simulation results and compares the performance of the proposed method with traditional approaches; and Section 6 concludes the paper with a summary of findings, contributions, and future research directions.

2. Literature Review

The integration of DG units into modern power grids has led to significant advancements and challenges in MGs. Ensuring adequate voltage regulation and optimal power sharing among parallel−connected generators is a critical issue in MGs. Droop control methods have emerged as a fundamental solution due to their ability to distribute power without centralized control.

2.1. Traditional Droop Control Methods

Traditional droop control adjusts voltage amplitude and frequency automatically based on network load, allowing for equitable power distribution without the need for complex centralized communication. This simplicity and robustness make droop control particularly advantageous for MGs. However, traditional droop control methods often suffer from several limitations:

- **Inaccurate power sharing due to line impedance variations:** Traditional droop control assumes identical line impedances between DG units and loads. In practice, line impedances can vary significantly, leading to unequal voltage drops and phase shifts, causing inaccuracies in active and reactive power sharing among DG units.
- **Voltage and frequency deviations under load changes:** fixed droop coefficients cannot adapt quickly to sudden fluctuations in load demand, resulting in significant voltage and frequency deviations, compromising power quality and system stability.

- **Limited adaptability to dynamic operating conditions:** traditional methods lack the ability to adjust control parameters in real time, making them ineffective under changing load demands and network configurations.
- **Sensitivity to nonlinear loads and harmonics:** traditional droop control does not effectively handle nonlinear loads, leading to increased Total Harmonic Distortion (THD) and degraded power quality.
- **Dependence on communication links:** enhancements to traditional droop control often rely on communication between DG units, which can reduce system reliability and increase implementation complexity.

2.2. Advanced Droop Control Techniques

To overcome the limitations of conventional droop control, several advanced strategies have emerged. Adaptive droop control adjusts coefficients in real time based on system conditions, enhancing performance under varying loads and network configurations [7,8]. Virtual impedance control improves power sharing and stability by virtually modifying inverter output impedance [9]. Hierarchical control strategies utilize multi−layered control (primary, secondary, tertiary) for better coordination across microgrid levels [4]. Model Predictive Control (MPC) leverages predictive models to optimize future control actions, supporting proactive power management [10]. Lastly, distributed cooperative control strategies rely on real−time communication between DG units to reach consensus, improving performance and synchronization [11].

Despite their benefits, these advanced methods face several limitations beyond communication dependency. Many of them, such as adaptive and cooperative strategies, demand high computational resources and intricate system models to operate effectively, making real−world implementation challenging and costly. For instance, methods like MPC require significant computational power for real−time predictive analysis, which can be impractical in resource−constrained environments. Similarly, communication reliance increases the risk of instability in case of delays or failures, reducing system reliability. Moreover, the need for complex parameter tuning in adaptive and hierarchical methods can add considerable setup and maintenance complexity, hindering scalability and long−term usability [12–16].

The proposed ANN−PSO droop control strategy uniquely addresses these challenges with a decentralized design that eliminates the need for communication links and minimizes computational demands. By using offline particle swarm optimization (PSO) to generate optimal control inputs, the method enables responsive and adaptive real−time control without the resource−intensive burden of online computation. This approach not only simplifies implementation and enhances reliability but also maintains robust stability and power−sharing precision under dynamic conditions, setting it apart from other advanced techniques.

2.3. Artificial Neural Networks in Microgrid Control

ANN offers a promising solution by modeling nonlinear systems and providing adaptive control. ANN can adapt to changing conditions in real time, offering a more flexible and efficient control mechanism compared with traditional methods [17]. However, their implementation in MGs is challenged by high computational requirements and the need for extensive training datasets. Previous studies have applied ANN in various power system contexts, such as load forecasting, fault detection, and optimizing control parameters [18–21]. In these applications, PSO is often used to optimize the weights and biases of the ANN during training to enhance its predictive capabilities.

2.4. Particle Swarm Optimization in Power Systems

PSO is a robust optimization technique inspired by the social behavior of birds and fish, known for its simplicity and efficiency. It has been successfully applied to various power system problems, enhancing the performance of control strategies under diverse conditions [22–24]. Combining ANN with PSO presents a potential solution to overcome computational challenges, enabling real−time adaptive control in MGs.

2.5. Research Gap and Objectives

Despite these advancements, there remains a critical gap in effectively integrating ANN−based droop control strategies optimized with PSO for parallel−connected single−phase DG units in MGs. Existing methods do not fully address the need for real−time adaptation to load changes and line impedance variations, nor do they sufficiently validate their approaches under diverse operational scenarios. Previous hybrid ANN−PSO approaches often focus on optimizing the internal parameters of the ANN, such as weights and biases, during training. They may not address the specific issue of droop control optimization in MGs, particularly under varying line impedances and load conditions [4].

2.6. Contributions of the Proposed Method

This paper addresses the identified research gap by proposing a novel integration of ANN and PSO specifically for optimizing droop control inputs in MGs. Unlike prior methods, PSO is employed during the offline training phase to generate optimal dq−axis voltage reference values that compensate for transmission line effects and load variations. These optimized voltage references serve as the training data for the ANN, enabling it to learn the complex relationships between load conditions, line impedances, and the necessary control actions. By optimizing the control inputs rather than the ANN parameters, the method focuses on directly enhancing the control action for MG performance.

The proposed control strategy employs dq control for the single−phase inverter, which is critical in maintaining system stability under varying operating conditions. Through dq transformation, the active and reactive power components are decoupled, allowing for precise and independent management of power flow. The ANN, trained with dq voltage references generated offline by PSO, dynamically adjusts these parameters in real time, achieving stability even during rapid load changes and line impedance fluctuations. By learning complex, nonlinear relationships within the microgrid system, the ANN can predict and rectify power imbalances and voltage deviations efficiently, without the need for inter−unit communication. This adaptability significantly enhances system stability and responsiveness, outperforming conventional fixed−parameter droop control.

During real−time operation, the ANN rapidly computes the required control signals based on real−time measurements, ensuring the necessary responsiveness for MG applications. This approach decouples the optimization process from real−time operation, ensuring computational efficiency and effective control without the computational burden of online optimization.

The key contributions of this research include the following:

1. **Development of an innovative ANN−PSO strategy:** integrating ANN for adaptive control and PSO for optimization significantly advances control strategies for MGs, offering a novel application of these techniques specifically for droop control optimization.
2. **Enhanced real−time adaptation:** the proposed method adapts to real−time changes in the MG, improving power sharing precision under varying load conditions and line impedances without relying on communication links between DG units.
3. **Comprehensive evaluation under various scenarios:** The performance of the proposed method is evaluated under various scenarios, including different levels of RES integration, diverse line impedances (inductive, resistive, and mixed), and dynamic load changes (both linear and nonlinear). The results demonstrate that the

method maintains voltage and frequency stability, accurate power sharing, and acceptable THD levels across all tested conditions, outperforming conventional droop control methods.

4. **Scalability and practical implementation potential:** the approach's scalability and potential for practical implementation in larger MG systems with diverse renewable energy sources are discussed, highlighting its applicability in real−world settings.

By addressing the limitations of traditional droop control strategies and bridging the existing research gap, this method contributes to the development of more efficient and stable MG systems. The proposed intelligent control approach significantly improves MG performance by ensuring accurate power sharing, enhancing voltage and frequency stability, reducing harmonic distortions, and operating reliably without dependence on communication infrastructure.

3. Conventional Droop Control Method

3.1. Fundamental Control Mechanism

A primary challenge in the autonomous control of MGs is the regulation of voltage magnitude and frequency. This control relies on local measurements to ensure accurate power distribution in response to load changes, eliminating the need for communication among DG sources. It operates effectively in both isolated and grid−connected scenarios, facilitating smooth transitions between these states. The droop control strategy is widely used for integrating DG units within an MG, leveraging active and reactive power to modulate the inverter's output voltage and frequency using only local information. However, the dispersed placement of DGs, combined with line impedances and voltage variations, can lead to deviations from desired operational points, affecting optimal load distribution.

3.2. Overview of Droop Control

The droop control technique emulates the behavior of synchronous generators in traditional power systems by adjusting the terminal voltage frequency in response to active power changes and the terminal voltage amplitude in response to reactive power changes. This method is also utilized for managing parallel inverters in isolated MGs to autonomously allocate load demands. As depicted in Figure 1, a simplified model illustrates the power transfer via a transmission line from the micro−source to the load.

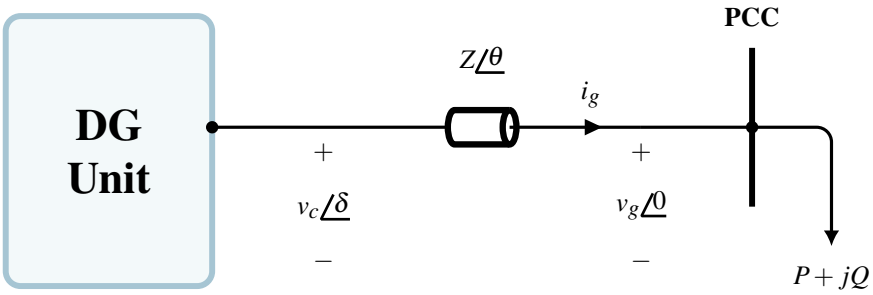

Figure 1. Simplified model of power transfer through a transmission line.

In this model, v_c represents the voltage at the inverter output after filtering, with a phase angle δ. The terminal voltage v_g appears after the line impedance $Z = R + jX = |Z|\angle\theta$, where R and X are the resistive and reactive components, respectively, and $\theta = \arctan\left(\frac{X}{R}\right)$ is the impedance angle. The complex power $S = P + jQ$ at the transmission line's end represents the active power P and reactive power Q delivered to the load.

The relationship between the voltages and the complex power is given by [25]

$$S = v_g i_g^* = \frac{v_c v_g}{Z}\angle(\delta - \theta) - \frac{v_g^2}{Z}\angle(-\theta) = P + jQ, \tag{1}$$

where i_g^* is the complex conjugate of the current i_g. By expressing the phasor relationships and separating real and imaginary parts, the active and reactive power can be approximated as [26]

$$\begin{aligned} P &= \frac{v_c}{R^2 + X^2}\left[R\left(v_c - v_g\cos(\theta)\right) + Xv_g\sin(\delta)\right] \\ Q &= \frac{v_c}{R^2 + X^2}\left[X\left(v_c - v_g\cos(\theta)\right) - Rv_g\sin(\delta)\right] \end{aligned} \tag{2}$$

Assuming that the voltage phase angle difference δ is small ($\delta \approx 0$), the trigonometric functions can be approximated as $\cos(\delta) \approx 1$ and $\sin(\delta) \approx \delta$. This simplifies the expressions for P and Q.

3.2.1. Scenario 1: Inductive Line Impedance ($\theta \approx 90°$)

In this scenario, the inductive component of the line impedance is significantly greater than the resistive component ($X \gg R$), so the resistive component can be neglected. The impedance angle θ approaches 90°. The simplified expressions for active and reactive power become

$$\begin{aligned} P &\approx \frac{v_c v_g}{X}\sin(\delta) \approx \frac{v_c v_g}{X}\delta, \\ Q &\approx \frac{v_c v_g}{X}\cos(\delta) - \frac{v_g^2}{X} \approx \frac{v_c v_g}{X} - \frac{v_g^2}{X}. \end{aligned} \tag{3}$$

The partial derivatives of P and Q with respect to δ and v_c are:

$$\begin{aligned} \frac{\partial P}{\partial \delta} &= \frac{v_c v_g}{X}, & \frac{\partial P}{\partial v_c} &= \frac{v_g \delta}{X} \\ \frac{\partial Q}{\partial \delta} &= 0, & \frac{\partial Q}{\partial v_c} &= \frac{v_g}{X} \end{aligned} \tag{4}$$

Equation (4) indicates that active power P can be controlled by adjusting the phase angle δ, while reactive power Q can be controlled by adjusting the voltage magnitude v_c. To achieve power sharing among parallel−connected DGs, droop characteristics utilizing active power versus frequency (P–f) and reactive power versus voltage (Q–V) are employed, as shown in Figure 2.

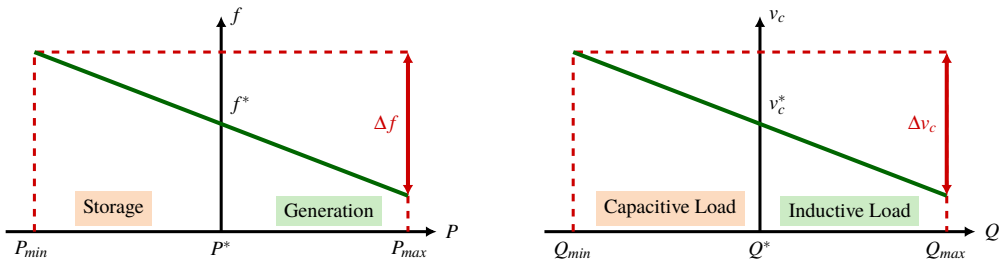

Figure 2. Droop characteristics for inductive line impedance.

The droop control expressions for an inductive MG are given by:

$$\begin{aligned} f &= f^* - f_p(P - P^*), \\ v_c &= v_c^* - v_q(Q - Q^*), \end{aligned} \tag{5}$$

where P^* and Q^* are the rated active and reactive power of the DG unit, f^* and v_c^* are the rated frequency and voltage amplitude, C_p, and C_q are the droop coefficients for frequency and voltage, respectively. The droop control scheme based on (5) is depicted in Figure 3.

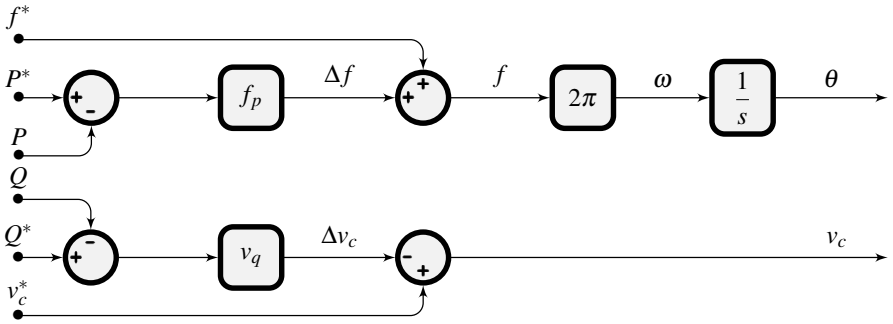

Figure 3. CDC scheme for inductive line impedance.

3.2.2. Scenario 2: Resistive Line Impedance ($\theta \approx 0°$)

In this scenario, the resistive component of the line impedance is much greater than the inductive component ($R \gg X$), so the inductive component can be neglected. The impedance angle θ approaches 0°. The simplified expressions for active and reactive power become

$$\begin{aligned} P &\approx \frac{v_c v_g}{R}\cos(\delta) - \frac{v_g^2}{R} \approx \frac{v_c v_g}{R} - \frac{v_g^2}{R}, \\ Q &\approx \frac{v_c v_g}{R}\sin(\delta) \approx \frac{v_c v_g}{R}\delta. \end{aligned} \tag{6}$$

The partial derivatives are

$$\begin{aligned} \frac{\partial P}{\partial \delta} &= 0, & \frac{\partial P}{\partial v_c} &= \frac{v_g}{R}, \\ \frac{\partial Q}{\partial \delta} &= \frac{v_c v_g}{R}, & \frac{\partial Q}{\partial v_c} &= \frac{v_g \delta}{R}. \end{aligned} \tag{7}$$

Equation (7) shows that active power P can be controlled by adjusting the voltage magnitude v_c, while reactive power Q can be controlled by adjusting the phase angle δ. To achieve power sharing between DGs operating in parallel, droop characteristics utilizing active power versus voltage (P–v_c) and reactive power versus frequency (Q–f) are employed, as demonstrated in Figure 4.

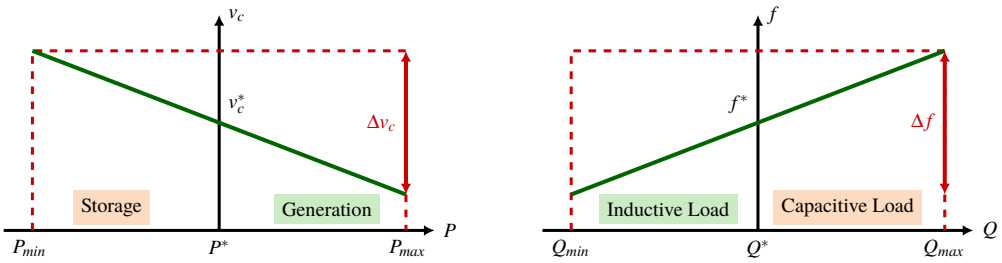

Figure 4. Droop characteristics for resistive line impedance.

The droop control expressions for a resistive MG are given by

$$\begin{aligned} f &= f^* - f_q(Q - Q^*), \\ v_c &= v_c^* - v_p(P - P^*). \end{aligned} \tag{8}$$

The droop control scheme based on (8) is illustrated in Figure 5.

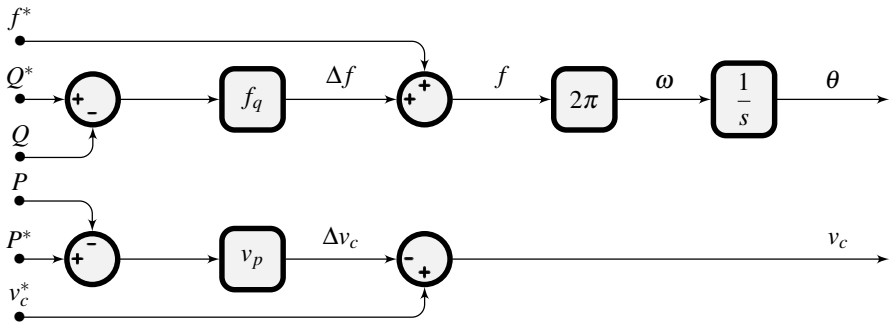

Figure 5. CDC scheme for resistive line impedance.

3.2.3. Scenario 3: Mixed−Line Impedance

In low−voltage MGs, both inductive and resistive components of line impedance significantly impact power distribution. The interdependence of active and reactive power affects both voltage and frequency, necessitating a more flexible control approach. Traditional droop control methods adjust voltage and frequency based on static coefficients, but these coefficients can limit the flexibility of the droop curve and result in discrepancies in power distribution if not appropriately selected.

To address this, a rotation matrix T is introduced to transform active and reactive powers (P, Q) into new components (P_r, Q_r), providing a more adaptable control mechanism (9). The transformation is given by

$$\begin{bmatrix} P_r \\ Q_r \end{bmatrix} = \begin{bmatrix} \cos(\phi) & -\sin(\phi) \\ \sin(\phi) & \cos(\phi) \end{bmatrix} \begin{bmatrix} P \\ Q \end{bmatrix}, \tag{9}$$

where $\phi = \theta$. The transformed power components become:

$$\begin{aligned} P_r &= \frac{R}{Z}P + \frac{X}{Z}Q, \\ Q_r &= -\frac{X}{Z}P + \frac{R}{Z}Q. \end{aligned} \tag{10}$$

Assuming a small phase angle difference δ, applying the rotation matrix simplifies the control relationships:

$$\begin{aligned} P_r &\approx \frac{v_c v_g}{Z}\cos(\delta - \theta) - \frac{v_g^2}{Z}\cos(\theta), \\ Q_r &\approx \frac{v_c v_g}{Z}\sin(\delta - \theta) - \frac{v_g^2}{Z}\sin(\theta). \end{aligned} \tag{11}$$

When resistance and reactance are comparable ($R \approx X$), both P and Q are affected by δ and v_c, linking all four control variables. In such cases, decoupling is necessary to ensure precise and independent control of power flows. This analysis illustrates the complexity of power coupling in low−voltage MGs and underscores the need for advanced control techniques to handle the nonlinear interactions between voltage, frequency, and power components effectively.

4. Proposed Droop Control Method

This section presents a novel methodology for droop control in MGs, utilizing an artificial neural network droop control (ANNDC) technique, as shown in Figure 6. The goal is to improve the performance of inverter−based MGs, ensuring stable and efficient operation under varying load conditions. PSO is employed to fine−tune the parameters of the ANN and generate a comprehensive dataset for ANN training.

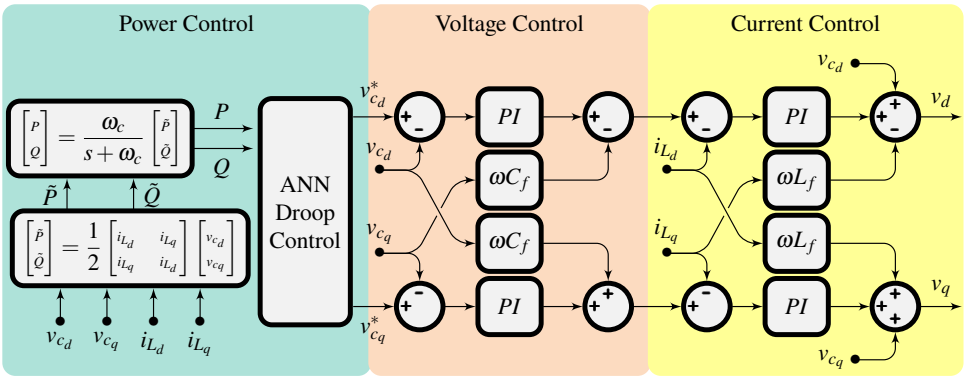

Figure 6. Structure of the proposed droop control.

The proposed method aims to address the limitations of traditional droop control strategies by incorporating intelligent control techniques. By integrating ANN and PSO, the control system can adaptively adjust to changing operating conditions, enhancing overall system performance.

4.1. Structure of the Proposed Control for DG Unit

Transitioning from the broader concept of MGs, the specific control structure employed in this paper is illustrated in Figure 7. This structure forms the foundation for the development and application of the proposed droop control methodology, as well as the implementation of the PSO and ANN algorithms.

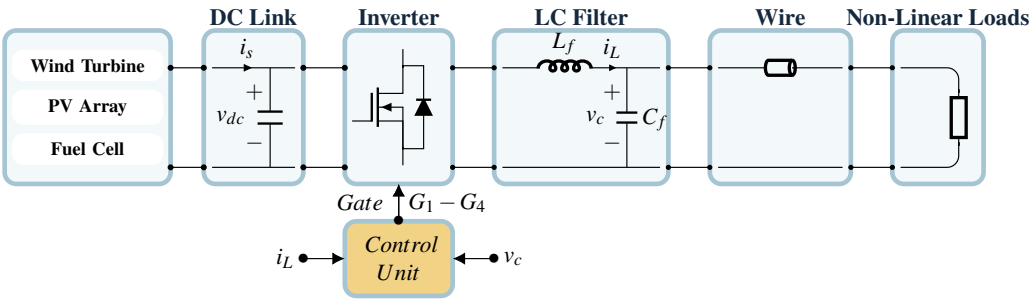

Figure 7. Structure of the distributed generator.

The DG inverter is connected to the load through a second−order LC filter, which plays a crucial role in attenuating the switching components of the Pulse Width Modulation (PWM) carrier voltages and limiting the current harmonics injected into the Point of Common Coupling (PCC). This setup is essential for maintaining power quality and ensuring compliance with grid codes.

In addition to the DG unit, the MG includes a nonlinear load representing typical conditions found in modern electrical grids. Including a nonlinear load allows for a more realistic representation of practical load conditions, ensuring that the proposed control method is robust and effective in real−world scenarios.

Figure 8 illustrates the robust control scheme for a DG unit within an MG, integrating traditional droop control with an ANNDC. This control method comprises three primary components: an ANNDC and two cascaded PI controllers for voltage and current control, respectively.

The ANNDC generates the decoupled *dq* voltage references, which are subsequently used by the inverter. The power control, managed by the ANN, ensures balanced power distribution. By leveraging the ANN's ability to learn complex nonlinear relationships, the control system can adapt to varying load conditions more effectively than traditional droop control methods.

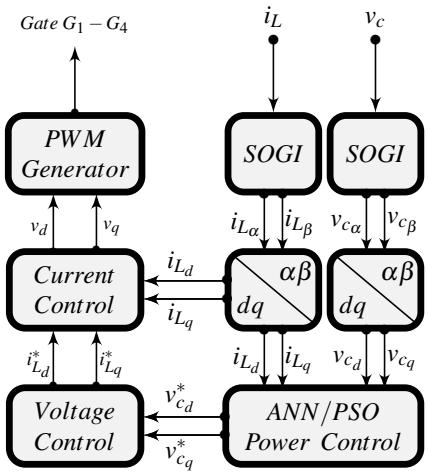

Figure 8. Structure of the proposed control unit.

The current control system generates v_{dq} for the PWM module, providing a fast, efficient response to filter inductor current fluctuations and harmonic disturbances. This significantly improves the Total Harmonic Distortion (THD) of the output current, enhancing power quality.

The integration of ANN and PSO in the control strategy represents a novel contribution to the field. Unlike CDC methods that rely on fixed droop coefficients, the proposed approach adaptively adjusts the droop coefficients based on the MG's operating conditions. This adaptability leads to improved performance and efficiency in power sharing among DG units.

By combining these control methods, MG performance is maintained while achieving high precision in active and reactive power control. This directly contributes to the overall objectives of enhancing system performance under varying load conditions and improving power quality.

4.2. dq Model for Single−Phase Inverter

The Park Transformation is a common tool used to model three−phase inverters. However, its application to single−phase inverters presents challenges due to the requirement of at least two orthogonal components, whereas a single−phase inverter only provides one component [27,28].

To address this issue, an imaginary component is generated based on the real component, effectively creating the required second orthogonal component. In this paper, a second−order generalized integrator (SOGI) is employed to achieve this [29]. The structure of the SOGI, as shown in Figure 9, takes the measurement of the single−phase AC component (x_a) as input, producing the estimated $\alpha\beta$ components (x_α and x_β) as output. It is important to note that x_α is identical to the input AC measured component, while x_β is shifted by 90° relative to x_α.

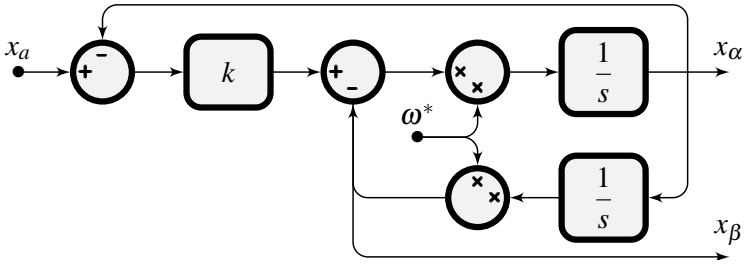

Figure 9. Structure of the second−order generalized integrator (SOGI).

Following this, the Park transformation is applied to the extracted $\alpha\beta$ components, resulting in the dq components (x_d and x_q). The state−space equation for the single−phase inverter is expressed as follows:

$$\begin{bmatrix} \dot{i}_L \\ \dot{v}_c \end{bmatrix} = \begin{bmatrix} -\frac{R_{L_f}}{L_f} & -\frac{1}{L_f} \\ \frac{1}{C_f} & -\frac{1}{Z.C_f} \end{bmatrix} \begin{bmatrix} i_L \\ v_c \end{bmatrix} + \begin{bmatrix} \frac{1}{L_f} \\ 0 \end{bmatrix} v \tag{12}$$

In this equation, the control variable v is determined by the state of the switches in the single−phase inverter. After applying the SOGI, the state−space representation becomes

$$\begin{bmatrix} \dot{i}_{L_\alpha} \\ \dot{i}_{L_\beta} \\ \dot{v}_{c_\alpha} \\ \dot{v}_{c_\beta} \end{bmatrix} = \begin{bmatrix} -\frac{R_{L_f}}{L_f} & 0 & -\frac{1}{L_f} & 0 \\ 0 & -\frac{R_{L_f}}{L_f} & 0 & -\frac{1}{L_f} \\ \frac{1}{C_f} & 0 & -\frac{1}{Z.C_f} & 0 \\ 0 & \frac{1}{C_f} & 0 & -\frac{1}{Z.C_f} \end{bmatrix} \begin{bmatrix} i_{L_\alpha} \\ i_{L_\beta} \\ v_{c_\alpha} \\ v_{c_\beta} \end{bmatrix} + \begin{bmatrix} \frac{1}{L_f} & 0 \\ 0 & \frac{1}{L_f} \\ 0 & 0 \\ 0 & 0 \end{bmatrix} \begin{bmatrix} v_\alpha \\ v_\beta \end{bmatrix} \tag{13}$$

Finally, by applying the dq rotating transformation, the dynamic equation for the single−phase inverter is obtained:

$$\begin{bmatrix} \dot{i}_{L_d} \\ \dot{i}_{L_q} \\ \dot{v}_{c_d} \\ \dot{v}_{c_q} \end{bmatrix} = \begin{bmatrix} -\frac{R_{L_f}}{L_f} & -\omega & -\frac{1}{L_f} & 0 \\ \omega & -\frac{R_{L_f}}{L_f} & 0 & -\frac{1}{L_f} \\ \frac{1}{C_f} & 0 & -\frac{1}{Z.C_f} & -\omega \\ 0 & \frac{1}{C_f} & \omega & -\frac{1}{Z.C_f} \end{bmatrix} \begin{bmatrix} i_{L_d} \\ i_{L_q} \\ v_{c_d} \\ v_{c_q} \end{bmatrix} + \begin{bmatrix} \frac{1}{L_f} & 0 \\ 0 & \frac{1}{L_f} \\ 0 & 0 \\ 0 & 0 \end{bmatrix} \begin{bmatrix} v_d \\ v_q \end{bmatrix} \tag{14}$$

By incorporating an imaginary component via the SOGI, it becomes possible to apply the Park Transformation for modeling a single−phase inverter. This, in turn, facilitates the development of an efficient control scheme based on the dq model, as shown in Figure 10.

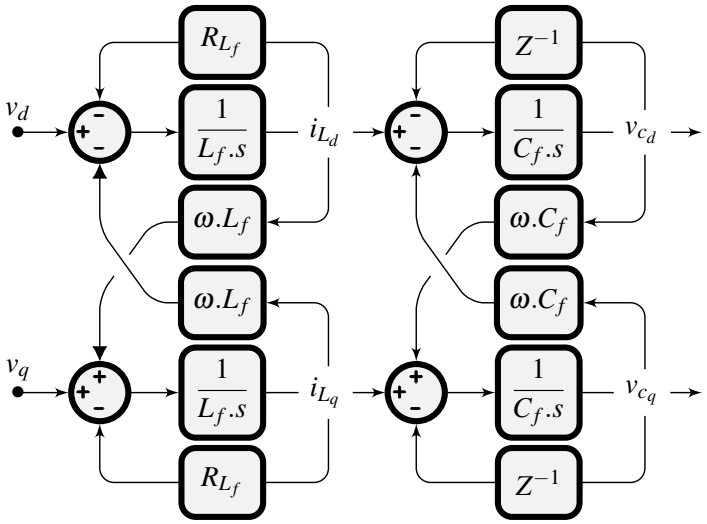

Figure 10. dq model of the single−phase inverter.

4.3. dq Control for Single−Phase Inverter

The design of the *dq* controller for a single−phase inverter is crucial for achieving high performance operation of the MG. Similar to a three−phase inverter, the control strategy consists of two cascaded Proportional−Integral (PI) controllers: an inner current control loop and an outer voltage control loop. Figure 11 illustrates the control structure of a single−phase inverter in the *dq* frame, where the *dq* voltage references are obtained from the ANN−based power controller.

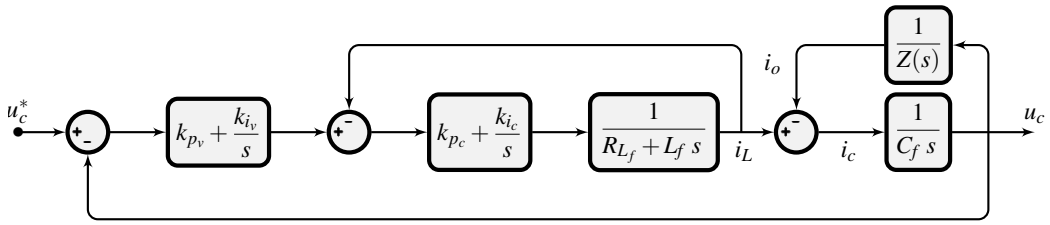

Figure 11. Control structure of the single−phase inverter in the *dq* frame.

To design the cascaded current and voltage loop PI controllers, the open−loop transfer functions (OLTF) and closed−loop transfer functions (CLTF) are derived. The objective is to achieve desired dynamic responses and stability margins by appropriately tuning the controller parameters.

4.3.1. Current Control Loop

The inner current control loop is responsible for regulating the filter inductor current $i_{L_{dq}}$ to follow the reference current provided by the voltage control loop. The structure of the current control loop is shown in Figure 11. The transfer function of the plant (inverter and filter) in the *dq* frame for the current control loop is given by

$$H_c(s) = \frac{1}{L_f s + R_{L_f}} \tag{15}$$

where L_f is the filter inductance and R_{L_f} is the resistance of the filter inductor.

The PI controller for the current loop is defined as

$$C_c(s) = k_{p_c} + \frac{k_{i_c}}{s} \tag{16}$$

where k_{p_c} and k_{i_c} are the proportional and integral gains, respectively.

The open−loop transfer function of the current control loop is

$$OLTF_c(s) = C_c(s) \cdot H_c(s) = \left(k_{p_c} + \frac{k_{i_c}}{s}\right) \cdot \frac{1}{L_f s + R_{L_f}} \tag{17}$$

To simplify the expression, the numerator and denominator are multiplied to obtain

$$OLTF_c(s) = \frac{k_{p_c} + \frac{k_{i_c}}{s}}{L_f s + R_{L_f}} = \frac{k_{i_c}}{s} \cdot \frac{1 + \frac{k_{p_c}}{k_{i_c}} s}{L_f s + R_{L_f}} \tag{18}$$

The objective is to cancel the pole introduced by the filter inductor L_f by selecting the controller gains appropriately. Setting

$$\frac{k_{p_c}}{k_{i_c}} = \frac{L_f}{R_{L_f}}, \tag{19}$$

this compensates for the dynamics of the inductor, simplifying the open−loop transfer function to

$$OLTF_c(s) = \frac{k_{i_c}}{s} \cdot \frac{1}{R_{L_f}} \tag{20}$$

The closed−loop transfer function of the current control loop is then

$$CLTF_c(s) = \frac{OLTF_c(s)}{1 + OLTF_c(s)} = \frac{\frac{k_{i_c}}{R_{L_f} s}}{1 + \frac{k_{i_c}}{R_{L_f} s}} = \frac{1}{1 + \frac{R_{L_f}}{k_{i_c}} s} \tag{21}$$

This represents a first−order system with a time constant τ_c:

$$CLTF_c(s) = \frac{1}{1 + \tau_c s}, \quad \text{where } \tau_c = \frac{R_{L_f}}{k_{i_c}} \tag{22}$$

To achieve the desired transient response, a suitable time constant τ_c is selected. Assuming a desired current loop response time T_{r_c}, it can be related to the time constant as $T_{r_c} = 3\tau_c$. Consequently, the integral gain is expressed as

$$k_{i_c} = \frac{3R_{L_f}}{T_{r_c}} \tag{23}$$

Using Equation (19), the proportional gain is

$$k_{p_c} = \frac{L_f}{R_{L_f}} k_{i_c} = \frac{3L_f}{T_{r_c}} \tag{24}$$

Thus, the PI controller gains for the current loop are

$$\begin{cases} k_{i_c} = \dfrac{3R_{L_f}}{T_{r_c}} \\ k_{p_c} = \dfrac{3L_f}{T_{r_c}} \end{cases} \tag{25}$$

By appropriately selecting T_{r_c}, the desired speed of response and stability for the current control loop can be ensured.

4.3.2. Voltage Control Loop

The outer voltage control loop regulates the inverter output voltage $v_{c_{dq}}$ to follow the reference voltage provided by the ANN−based power controller. The structure of the voltage control loop is also shown in Figure 11. The transfer function of the plant for the voltage control loop is

$$H_v(s) = \frac{1}{C_f s} \tag{26}$$

where C_f is the filter capacitance.

The PI controller for the voltage loop is defined as

$$C_v(s) = k_{p_v} + \frac{k_{i_v}}{s} \tag{27}$$

The open−loop transfer function of the voltage control loop is

$$OLTF_v(s) = C_v(s) \cdot H_v(s) = \left(k_{p_v} + \frac{k_{i_v}}{s}\right) \cdot \frac{1}{C_f s} \tag{28}$$

Simplification yields

$$OLTF_v(s) = \frac{k_{p_v}}{C_f s^2} + \frac{k_{i_v}}{C_f s^3} \tag{29}$$

However, the resulting expression indicates a third−order system, which complicates the controller design. To mitigate this issue, it is assumed that the inner current loop operates much faster than the outer voltage loop. Consequently, the current control loop can be approximated as a unity gain for the voltage loop design. This simplification enables the plant to be represented as a first−order system.

Rewriting the open−loop transfer function

$$OLTF_v(s) = \left(k_{p_v} + \frac{k_{i_v}}{s}\right) \cdot \frac{1}{C_f s}, \tag{30}$$

the closed−loop transfer function of the voltage control loop is

$$CLTF_v(s) = \frac{OLTF_v(s)}{1 + OLTF_v(s)} = \frac{\frac{k_{i_v}}{C_f s^2} + \frac{k_{p_v}}{C_f s}}{1 + \frac{k_{i_v}}{C_f s^2} + \frac{k_{p_v}}{C_f s}} \tag{31}$$

Normalizing the denominator yields

$$CLTF_v(s) = \frac{k_{i_v} + k_{p_v} s}{s^2 + \frac{k_{p_v}}{C_f} s + \frac{k_{i_v}}{C_f}} \tag{32}$$

Comparing this with the standard second−order system transfer function

$$CLTF_v(s) = \frac{\omega_n^2}{s^2 + 2\xi\omega_n s + \omega_n^2}, \tag{33}$$

the controller parameters can be obtained by equating coefficients

$$\begin{cases} \omega_n^2 = \frac{k_{i_v}}{C_f} \\ 2\xi\omega_n = \frac{k_{p_v}}{C_f} \end{cases} \tag{34}$$

where ω_n is the natural frequency and ξ is the damping coefficient (typically between 0.7 and 1 for a critically damped or slightly underdamped response).

Solving for the PI controller gains

$$\begin{cases} k_{i_v} = C_f \omega_n^2 \\ k_{p_v} = 2\xi C_f \omega_n \end{cases} \tag{35}$$

Selecting suitable values for ω_n and ξ enables the desired transient response and stability for the voltage control loop.

4.4. Power Sharing Control Loop

The inverter output voltage v_c and the filter inductor current i_L are measured and used to compute the instantaneous active and reactive power of the inverter. These quantities are transformed into the synchronous dq reference frame using the Park Transformation, resulting in v_{c_d}, v_{c_q}, i_{L_d}, and i_{L_q}.

The instantaneous active power $\tilde{P}$ and reactive power $\tilde{Q}$ can then be calculated using

$$\begin{bmatrix} \tilde{P} \\ \tilde{Q} \end{bmatrix} = \frac{1}{2} \begin{bmatrix} i_{L_d} & i_{L_q} \\ i_{L_q} & i_{L_d} \end{bmatrix} \cdot \begin{bmatrix} v_{c_d} \\ v_{c_q} \end{bmatrix} \tag{36}$$

These expressions are derived from the definition of instantaneous power in the dq frame, where $\tilde{P}$ represents the real power component and $\tilde{Q}$ represents the imaginary power component. The calculations utilize the orthogonality of the d and q axes and are essential for decoupling active and reactive power control.

To obtain the average active and reactive power components P and Q corresponding to the fundamental frequency, the instantaneous powers $\tilde{P}$ and $\tilde{Q}$ are passed through low−pass filters with a cutoff frequency ω_c:

$$\begin{bmatrix} P \\ Q \end{bmatrix} = \frac{\omega_c}{s + \omega_c} \begin{bmatrix} \tilde{P} \\ \tilde{Q} \end{bmatrix} \tag{37}$$

The choice of cutoff frequency ω_c is crucial for the system's dynamic response. It must be sufficiently low to effectively filter out high−frequency components and harmonics caused by switching actions and nonlinear loads, ensuring smooth signals for control purposes. However, ω_c should also be high enough to allow the controller to respond promptly to changes in power demand. Typically, ω_c is selected based on a trade−off between filtering effectiveness and system responsiveness, often set to a fraction of the fundamental frequency.

The power sharing between the inverters is accomplished using the ANNDC. The ANNDC calculates the voltage amplitude references $v^*_{c_d}$ and $v^*_{c_q}$, which are then applied to the voltage controller, as shown in Figure 6. By adjusting these voltage references, the ANNDC ensures balanced power distribution among the DG units in the MG, maintaining system performance.

4.5. Artificial Neural Network Droop Control

As illustrated in Figure 12, an artificial neural network (ANN) comprises layers of interconnected neurons, where each layer is fully connected with the preceding and succeeding layers. These layers include an input layer, where the input signals are fed, several hidden layers, and an output layer, which produces the final result.

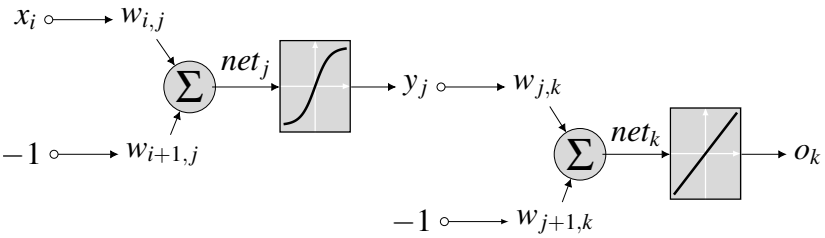

Figure 12. Structure of the ANN.

Each neuron in the ANN is characterized by a combination function and an activation function. The combination function performs a weighted sum of the signals from the neurons in the previous layer. The activation function introduces non−linearity into the response, mimicking the operation of a biological neuron. These parameters (weights and activation functions) facilitate the transformation of an input signal from the previous layer into an output signal for the next layer.

The design of the ANN involves five critical steps: input selection, data collection, ANN architecture selection, ANN training, and ANN testing. Each step is crucial and contributes to the successful implementation of the ANN.

In the proposed application, referred to as ANNDC, the input variables of the neural network are the inverter's active and reactive powers (P, Q). The output variables are the reference voltages supplied to the voltage controller ($v^*_{c_d}$, $v^*_{c_q}$). The architecture of the ANN consists of three layers: an input layer with two neurons, a hidden layer comprising N neurons with logarithmic sigmoid activation functions, and an output layer with two neurons using linear activation functions. This ANN architecture is specifically designed to accommodate the requirements of the ANNDC for effective droop control in MGs.

In the following subsections, the generation of the required training data for the ANN using PSO is discussed, followed by a detailed explanation of the training, testing, and validation process.

4.6. Particle Swarm Optimization

PSO plays a vital role in the proposed approach by generating the training data for the ANN. Unlike traditional applications where PSO is used to optimize the internal parameters of the ANN, in this method, PSO is employed during the offline training phase to generate optimal $dq-$axis voltage reference values. These optimized voltage references compensate for transmission line effects and load variations, enabling the ANN to learn the complex relationships between load conditions, line impedances, and the necessary control actions.

PSO is a stochastic optimization technique inspired by the social behavior of swarms in nature [22,23,30]. The underlying idea is that a collective of individuals, each with limited intelligence, can achieve complex global optimization through collaboration.

In the context of PSO, each individual, or "particle", represents a potential solution to the optimization problem. The particles explore the search space collectively, aiming to identify the global optimum. Initially, each particle is assigned a random position and velocity within the search space, and the quality of each particle's position is evaluated by a fitness function.

As the particles traverse the search space, they remember the best position they have encountered ($P^k_{\text{Best}_i}$), and they are also aware of the best position found by any particle in the swarm (G^k_{Best}).

The velocity of each particle is updated based on these two parameters, according to

$$v_{ij}^{k+1} = \omega\, v_{ij}^{k} + c_1 r_1 \left(P^k_{\text{Best}_{ij}} - x_{ij}^{k} \right) + c_2 r_2 \left(G^k_{\text{Best}_j} - x_{ij}^{k} \right), \tag{38}$$

with $j = 1, 2, \ldots, d$ and $i = 1, 2, \ldots, d$, where d is the dimension of the search space.

In Equation (38), the selection of c_1, c_2, r_1, and r_2 is based on standard PSO parameter settings. Typically, c_1 and c_2 are chosen to balance exploration and exploitation, often set to values like 1.49. The random variables r_1 and r_2 are uniformly distributed in the range [0,1], introducing stochastic behavior in the particle updates. The parameter ω, representing the inertia weight, is linearly decreased from 0.9 to 0.4.

Figure 13 illustrates the typical motion of a particle in an optimization problem.

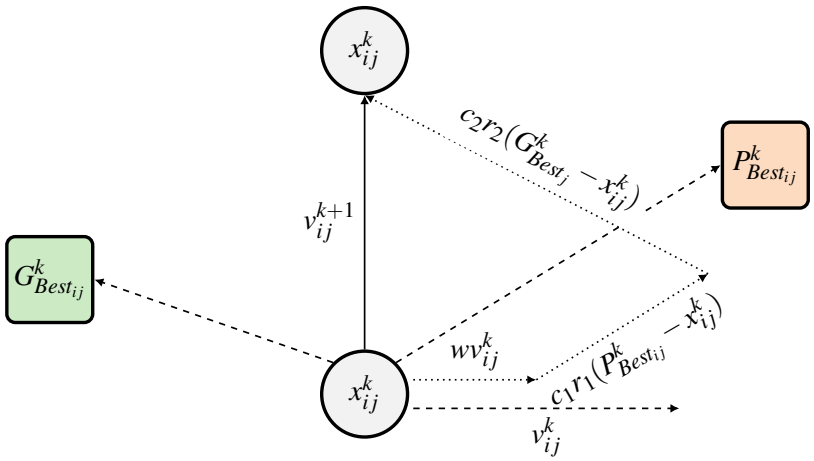

Figure 13. Displacement of particles in the search space.

PSO can be envisioned as a group of explorers searching for the best location in a vast landscape. Each explorer moves based on their own past experiences and learns from the discoveries of others, gradually converging on the most promising location. This process plays a critical role in the next step, where datasets are extracted to train the ANN.

Since PSO is utilized only during the offline training phase, its convergence speed does not affect the real−time performance of the MG control system. Once the ANN is trained using the dataset generated by PSO, it operates independently of the PSO algorithm during real−time control. The ANN can rapidly compute the required control signals based on real−time measurements, ensuring the necessary responsiveness for MG applications.

4.7. Extracting the Dataset for Training the ANN Using PSO

Following the setup of the ANN and PSO, the next crucial step involves extracting a dataset for training the ANN. In this context, the PSO algorithm is utilized to determine the optimal $dq-$axis voltage reference values $(v_{c_d}^*, v_{c_q}^*)$ to be applied to the voltage controller under different operating conditions, as depicted in Figure 14.

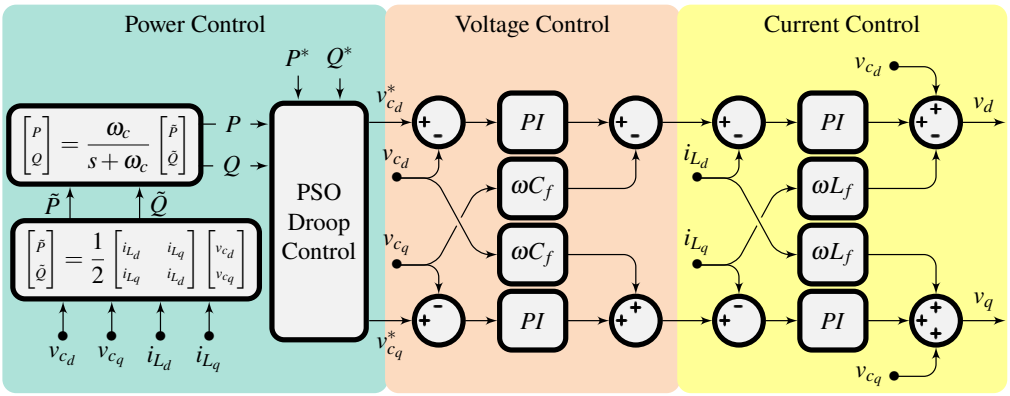

Figure 14. Structure of the proposed PSO−based droop control.

By optimizing the control inputs rather than the ANN parameters, the PSO algorithm generates a dataset of optimal control actions corresponding to different operating scenarios. This dataset captures the relationship between system states and the control inputs that achieve optimal performance, including compensation for transmission line effects and load variations.

This optimization process aims to minimize the fitness function f, while adhering to the operating constraints expressed as:

$$\begin{aligned} &\textbf{Fitness function:} \quad f(P,Q) = \frac{1}{2}\left((P-P^*)^2 + (Q-Q^*)^2\right) \\ &\textbf{Constraints:} \quad \begin{cases} 110\,\text{V} \leq v_c^* \leq 120\,\text{V} \\ 70\,\text{V} \leq v_{c_d}^* \leq v_c^* \\ 0\,\text{V} \leq v_{c_q}^* \leq \sqrt{v_c^{*2} - v_{c_d}^{*2}} \end{cases} \end{aligned} \tag{39}$$

The results of the data extraction process based on PSO are visualized in Figure 15.

This dataset encompasses a wide range of operating points and serves as a comprehensive training set for the ANN. The aim is to ensure that the ANN can effectively learn and generalize from a representative sample of the MG's operating conditions. By providing clear definitions of the fitness function and constraints, the reproducibility of this process is enhanced, enabling other researchers to apply similar techniques in their own studies on MGs.

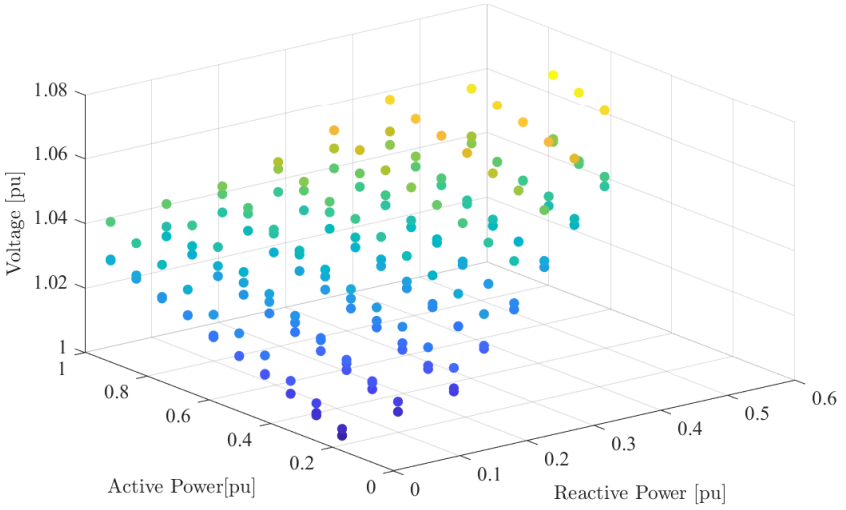

(**a**) d−axis

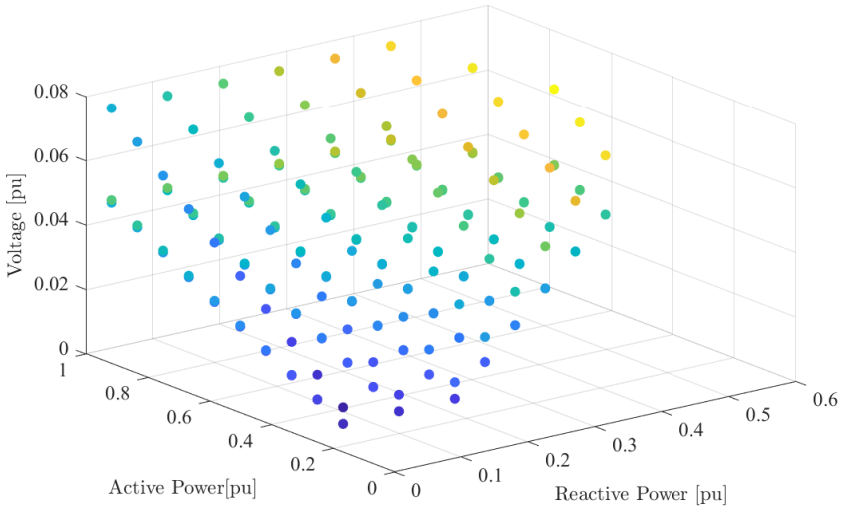

(**b**) q−axis

Figure 15. PSO data training.

4.8. Training, Testing, and Validation of the ANN

After establishing the dataset, the next phase involves training, testing, and validating the ANN. This phase ensures the practical effectiveness of the model and its ability to generalize beyond the training data, thus avoiding overfitting.

The central idea behind the ANN's functionality lies in the careful adjustment of its weights and biases, achieved through an iterative learning process. This training phase utilizes the stochastic gradient descent backpropagation algorithm to regulate the weights of each neuron, guided by the error between the network's predicted output and the actual output. The learning process typically concludes when this error reaches a predefined acceptable threshold.

It is important to emphasize that the creation of an extensive and representative dataset is vital for the training of the ANN. In this research, the dataset was generated through simulations conducted under various operating conditions, including different levels of renewable energy source integration, diverse line impedances (inductive, resistive, and mixed), and dynamic load changes (both linear and nonlinear), as depicted in Figure 15. This comprehensive dataset provides valuable insights into the performance and characteristics of the MG, serving as a valuable resource for training and validating the ANN−based droop control strategy.

The simulation parameters are presented in Table 1.

Table 1. System parameters.

Power Parameters	Value
DC Link Voltage	240 V
DC Link Capacitor	3 mF
DG Output Apparent Power	600 VA
Inverter Switching Frequency	20 kHz
Nominal Output Voltage	120 V (rms)
Filter Inductance L_f, R_{L_f}	3 mH, 0.25 Ω
Filter Capacitor C_f	20 μF
Nominal Output Frequency	60 Hz
Sampling Step T_s	20 μs

Subsequently, the generated dataset was divided into ten subsets. Out of these subsets, eight were randomly selected to form the training dataset, while the remaining two were set aside for validation and testing purposes. To enhance the generalization ability of the ANN and minimize the risk of overfitting, this process was repeated ten times using different combinations of training, validation, and testing subsets.

Upon completion of the training, validation, and testing stages, a total of ten ANNs were available for evaluation. The selection of the final ANN was based on the performance of each model, as assessed by the Mean Squared Error (MSE) across all three stages. The choice was determined by either the individual MSEs or the sum of the MSEs, considering that the error variance among the different solutions was negligible. This approach ensured the selection of the most reliable and robust model for the study, guaranteeing the accuracy and effectiveness of the ANN−based droop control strategy.

By training the ANN with the optimized control actions generated by PSO, the ANN learns to map the system measurements (such as power demands and line conditions) to the optimal dq voltage references. During real−time operation, the ANN can rapidly generate appropriate control inputs based on the current system state without the need for online optimization. This results in a control strategy that is both adaptive and computationally efficient.

5. Results and Discussion

The simulation and analysis of low−voltage MGs are essential for validating control strategies and ensuring a reliable, high−quality power supply. This section presents the evaluation of the proposed ANNDC method compared with the CDC technique. Simulations were conducted using MATLAB/Simulink on two primary MG configurations: common bus and mesh grid structures.

5.1. Simulation Setup

5.1.1. Microgrid Configurations

Common Bus Structure

The common bus structure is a widely used topology in MGs, where DG units are connected in parallel to a common bus that feeds various loads. This configuration allows for efficient power distribution while maintaining system stability and power quality.

Figure 16 illustrates the common bus MG configuration used in the simulations. Four DG units, each rated at 600 VA with a voltage of 110 V and a frequency of 60 Hz, are connected to the common bus. The line impedances are modeled as series RL components with different characteristics: inductive and mixed. The specific parameters of these impedances are summarized in Table 2.

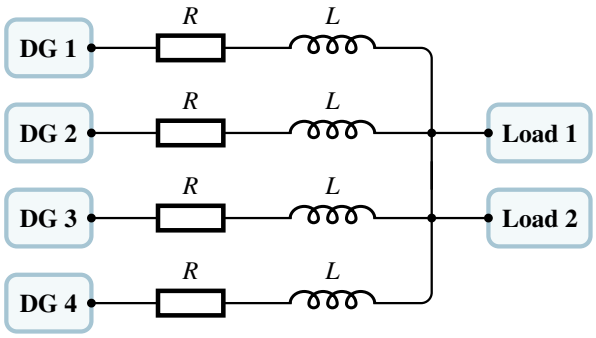

Figure 16. Microgrid configuration with a common bus structure.

Table 2. Line impedance parameters for different configurations.

	Inductive	Mixed
R, L	0.75 Ω, 4 mH	0.75 Ω, 2 mH

Mesh Grid Structure

The mesh grid structure offers increased flexibility and redundancy in power distribution, enhancing the resilience and reliability of the MG. In this topology, DG units are interconnected through multiple paths, allowing for better management in case of failures in network elements.

Figure 17 depicts the mesh grid MG configuration used in the simulations, where four DG units are interconnected to form a mesh network. Simulations were performed with line impedances of inductive and mixed nature. The parameters of these impedances are provided in Table 3.

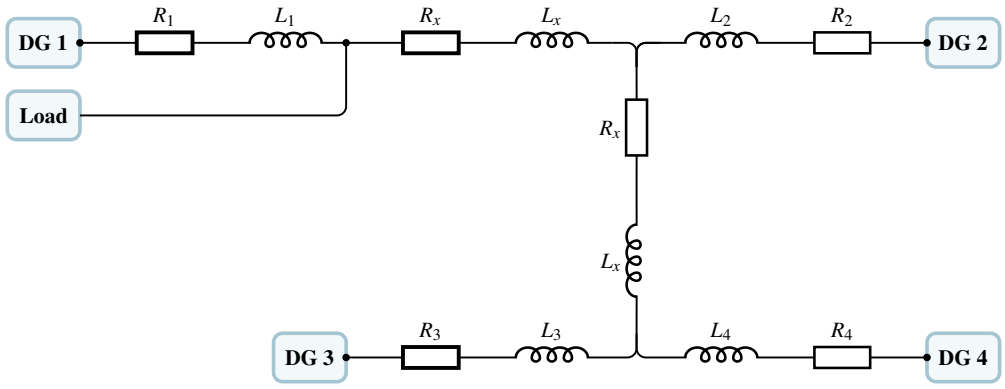

Figure 17. Microgrid configuration with a mesh grid structure.

Table 3. Line impedance parameters for different mesh grid configurations.

	Inductive	Mixed
R_1, L_1	0.75 Ω, 4.0 mH	0.75 Ω, 2.0 mH
R_2, L_2	0.60 Ω, 3.5 mH	0.75 Ω, 1.7 mH
R_3, L_3	0.60 Ω, 3.0 mH	0.60 Ω, 1.6 mH
R_4, L_4	0.50 Ω, 3.5 mH	0.60 Ω, 1.8 mH
R_x, L_x	0.75 Ω, 0.4 mH	0.75 Ω, 0.2 mH

5.1.2. Load Types and Test Scenarios

To evaluate the robustness and effectiveness of the proposed control method under various conditions, simulations were conducted using different load types and test scenarios.

Linear Loads

Simulations with linear loads were performed to assess the controller's ability to maintain system stability and efficient power sharing under varying load conditions. The loads used in the mesh grid structure are illustrated in Figure 18 and consist of the following:

- Load 1: 1.2 kW and 0 kVAR, connected continuously.
- Load 2: 1.2 kW and 1.2 kVAR, connected from 2 to 4 s.

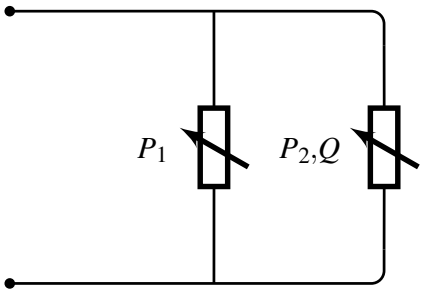

Figure 18. Linear loads in the mesh grid structure.

This scenario introduces dynamic changes to the system, allowing evaluation of the controller's response to load variations.

Nonlinear Loads

To test the controller's performance under more complex load conditions, simulations were conducted with nonlinear loads as shown in Figure 19:

- Load 1: 1.2 kW and 0 kVAR, connected continuously.
- Load 2: 0 kW and 1.2 kVAR, connected from 2 to 4 s.
- Load 3: A DC load consuming 10 A, connected from 2 to 4 s.

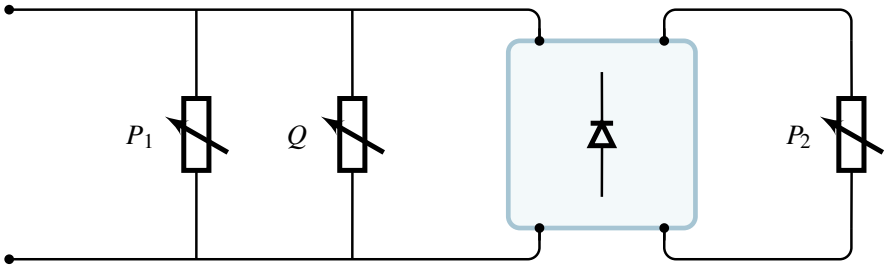

Figure 19. Nonlinear loads in the mesh grid structure.

These nonlinear loads introduce additional disturbances, testing the controller's ability to manage power quality, mitigate harmonics, and maintain voltage and frequency stability.

5.2. Simulation Results and Analysis

This section presents the simulation results and analysis of the proposed ANNDC method compared with the CDC technique. Key performance metrics evaluated include voltage magnitude stability, frequency stability, power−sharing accuracy among DG units, and the ability to handle harmonic distortions introduced by nonlinear loads.

5.2.1. Common Bus Structure

In the common bus MG configuration with linear loads, the performance of the ANNDC method was assessed under inductive and mixed−line impedance conditions. The objective was to evaluate the controller's effectiveness in maintaining voltage and frequency stability and ensuring accurate power sharing among DG units.

Figures 20c,d and 21c,d depict the active and reactive power outputs of each DG unit under inductive and mixed−line impedance conditions. Each DG unit supplies

approximately one quarter of the total power demanded by the load, demonstrating balanced power sharing. While both the CDC and the proposed ANNDC method perform adequately in terms of power sharing, the ANNDC method achieves more precise power distribution among the DG units. Specifically, the ANNDC method attains a power−sharing error of less than 0.5%, whereas the CDC method exhibits errors of up to 7%. This improvement is attributed to the ANNDC's ability to adjust control parameters in real time, effectively compensating for variations in line impedance and load conditions.

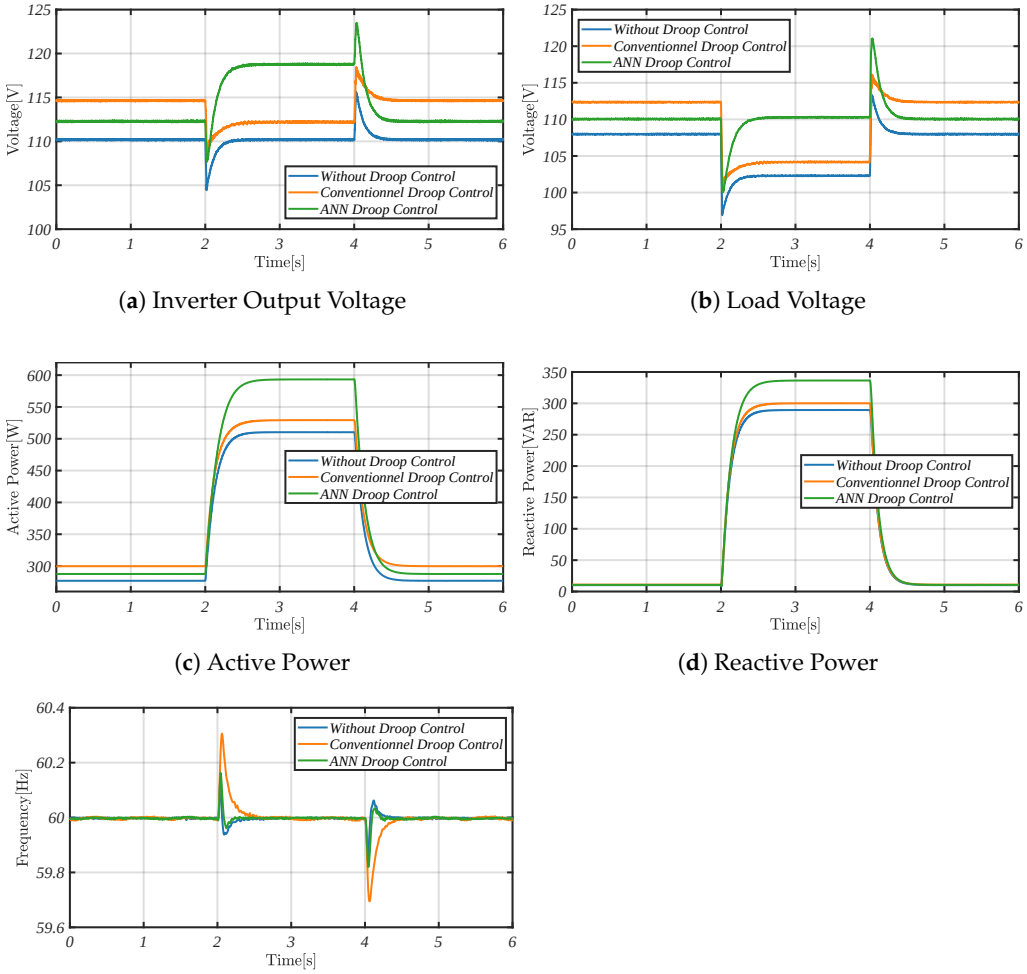

(**a**) Inverter Output Voltage

(**b**) Load Voltage

(**c**) Active Power

(**d**) Reactive Power

(**e**) Inverter Output Frequency

Figure 20. Simulation results of four DGs with inductive wire.

Figures 20b and 21b show the load voltage magnitude over time under inductive and mixed−line impedance conditions, respectively, after load variation. The ANNDC method maintains the load voltage magnitude within ±0.05 V of the nominal 100 V, whereas the CDC method exhibits deviations of up to ±5 V. This significant improvement in voltage regulation enhances the power quality delivered to the load.

Similarly, Figures 20e and 21e present the system frequency over time. The ANNDC method achieves better frequency stability, maintaining an average deviation of only 0.15 Hz from the nominal 60 Hz, compared with deviations of up to 0.4 Hz with the CDC method. Improved frequency stability is crucial for the proper functioning of sensitive equipment and overall system reliability.

As illustrated in Figures 20 and 21, the ANNDC method responds effectively to load variations by dynamically adjusting the voltage references on the *dq* axes, keeping the load voltage stable around its nominal value. This adaptive response enhances the overall efficiency of the MG, ensuring a reliable power supply under varying operating conditions.

In summary, the ANNDC method demonstrates superior performance over the CDC technique in the common bus configuration. By achieving more precise power sharing and maintaining tighter control over voltage and frequency, the ANNDC method enhances the reliability and power quality of MG operations.

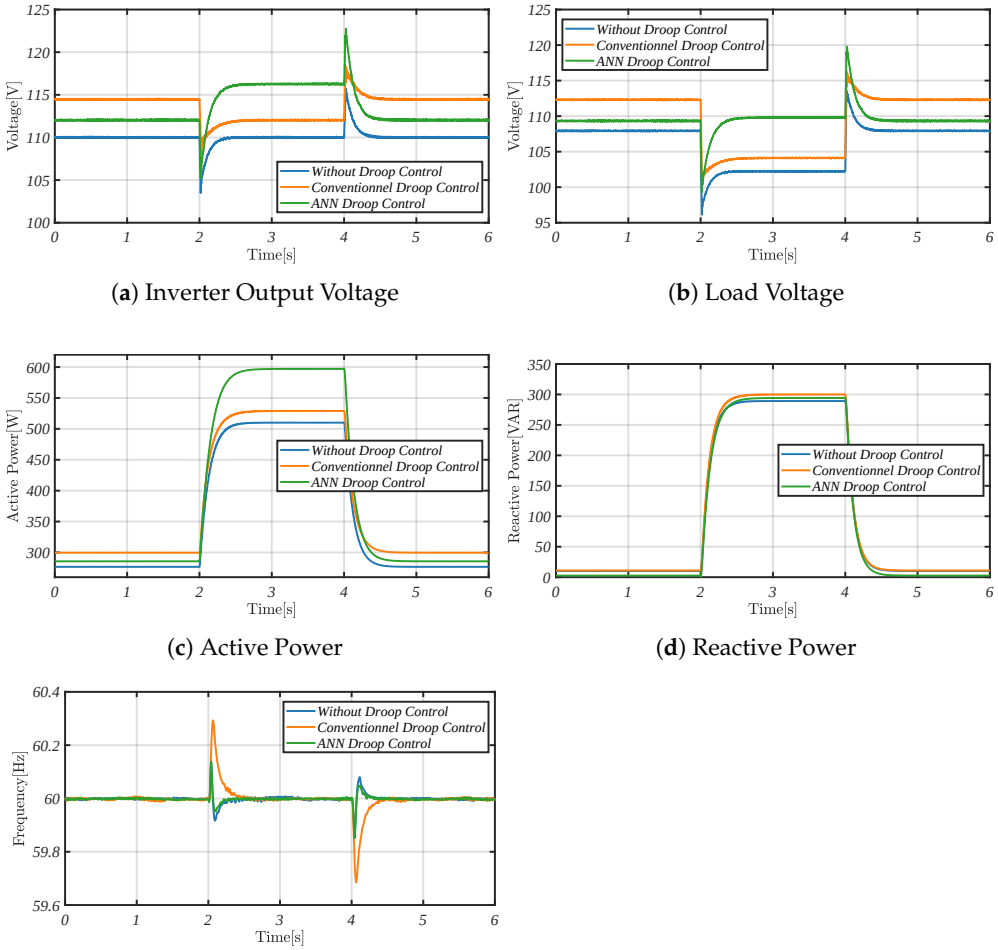

(**a**) Inverter Output Voltage (**b**) Load Voltage

(**c**) Active Power (**d**) Reactive Power

(**e**) Inverter Output Frequency

Figure 21. Simulation results of four DGs with mixed wire.

5.2.2. Mesh Grid Structure

The performance of the ANNDC method in the mesh MG configuration with linear and nonlinear loads was assessed under inductive and mixed−line impedance conditions. The evaluation focused on the controller's effectiveness in maintaining voltage and frequency stability, ensuring accurate power sharing among DG units, and reducing harmonic distortions in a complex network with nonlinear loads.

Figure 22 illustrate the load voltage magnitude over time under inductive and mixed−line impedance conditions, respectively, following load variations. The ANNDC method maintains the load voltage magnitude within ±0.2 V of the nominal 100 V, whereas the CDC (CDC) method exhibits deviations of up to ±4.5 V. Similarly, Figures 23d, 24d, 25d and 26d present the system frequency over time, showing that the ANNDC method achieves better frequency stability with an average deviation of only 0.15 Hz from the nominal 60 Hz, compared with deviations of up to 0.4 Hz with the CDC method.

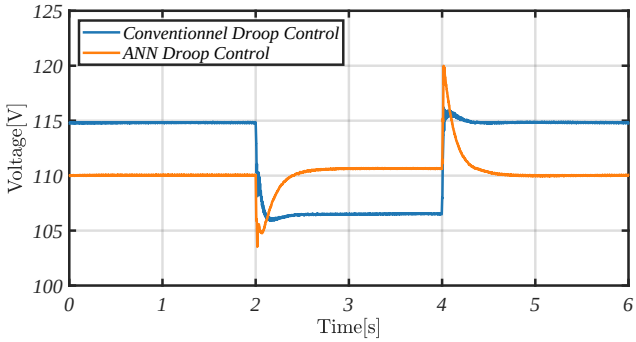

Figure 22. Load Voltage.

Accurate power sharing among DG units is critical for balanced MG operation. Figures 23b,c 24b,c, 25b,c and 26b,c depict the active and reactive power outputs of each DG unit under inductive and mixed−line impedance conditions. The ANNDC method achieves a power−sharing error of less than 1%, while the CDC method exhibits errors of up to 8%. This improvement is attributed to the ANNDC's real−time adjustment capabilities, effectively compensating for variations in line impedance and load conditions.

In this configuration, the DG1 supplies a larger portion of active power because it is electrically closer to the load compared with the DG4. Consequently, when the line impedances differ, the DG units generate different amounts of active power. Equal sharing of reactive power is not guaranteed among the DGs due to voltage variations throughout the MG caused by voltage drops across line impedances with different values.

As shown in Figures 24 and 26, the ANNDC method responds effectively to the introduction of nonlinear loads by adjusting the voltage references on the *dq* axes in real time, maintaining the load voltage stability around its nominal value. The ANNDC strategy demonstrates significant performance improvements over the CDC method across various operating conditions, including linear, nonlinear, and mixed impedance scenarios.

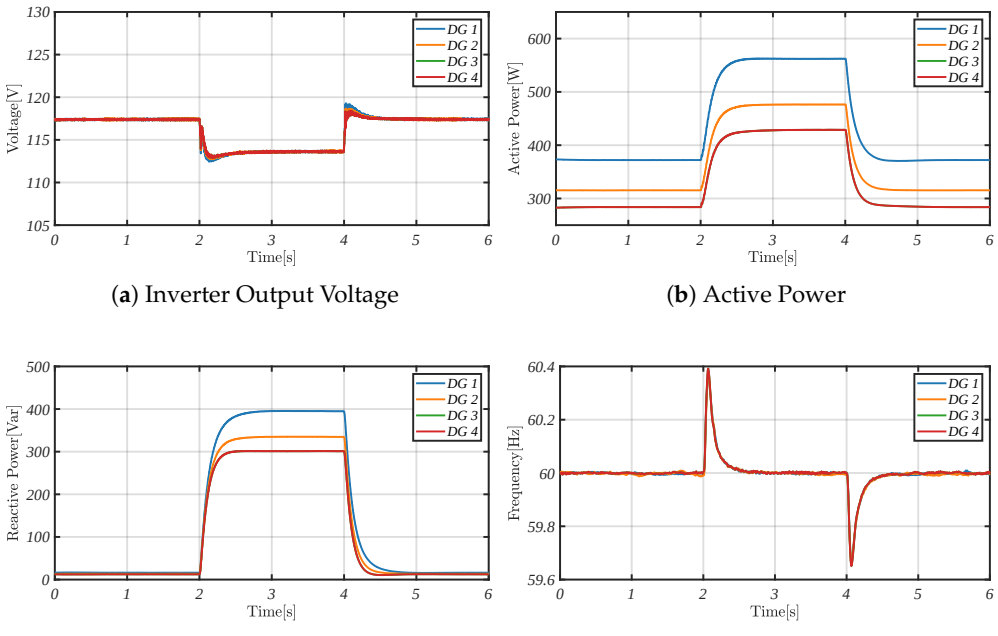

(**a**) Inverter Output Voltage

(**b**) Active Power

(**c**) Reactive Power

(**d**) Inverter Output Frequency

Figure 23. Simulation results of four DGs with inductive wire using CDC.

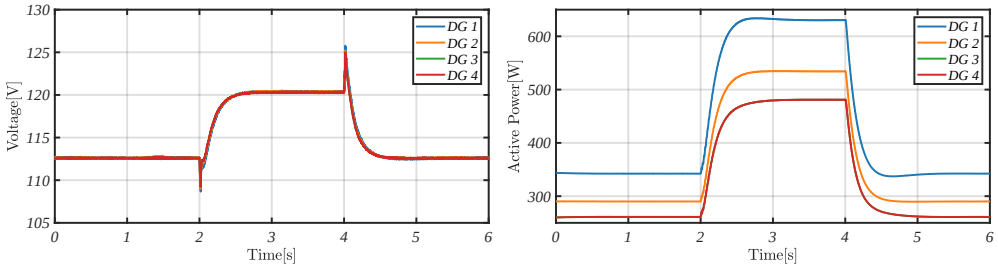

(**a**) Inverter Output Voltage

(**b**) Active Power

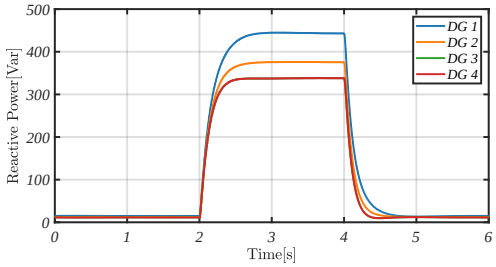

(**c**) Reactive Power

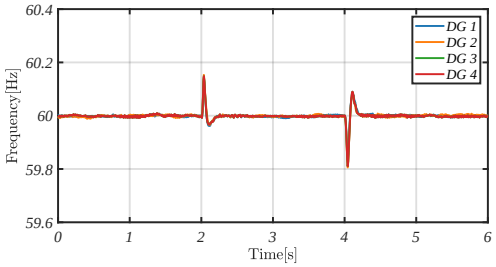

(**d**) Inverter Output Frequency

Figure 24. Simulation results of four DGs with inductive wire using proposed droop control.

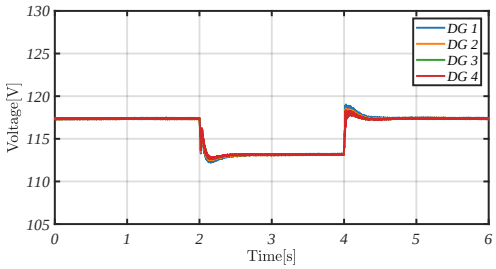

(**a**) Inverter Output Voltage

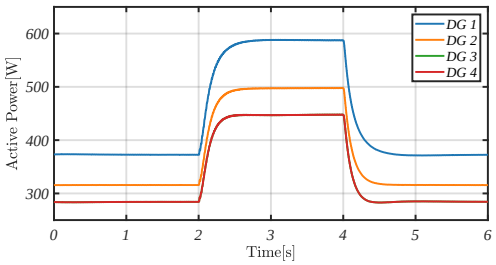

(**b**) Active Power

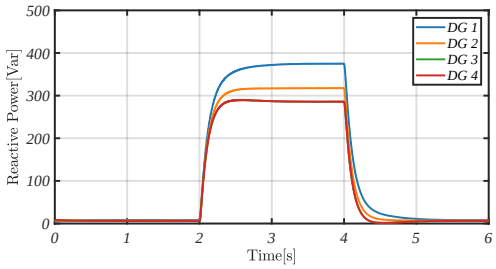

(**c**) Reactive Power

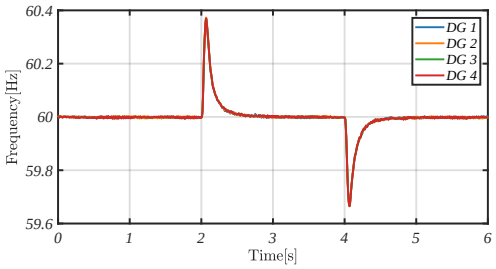

(**d**) Inverter Output Frequency

Figure 25. Simulation results of four DGs with mixed wire using CDC.

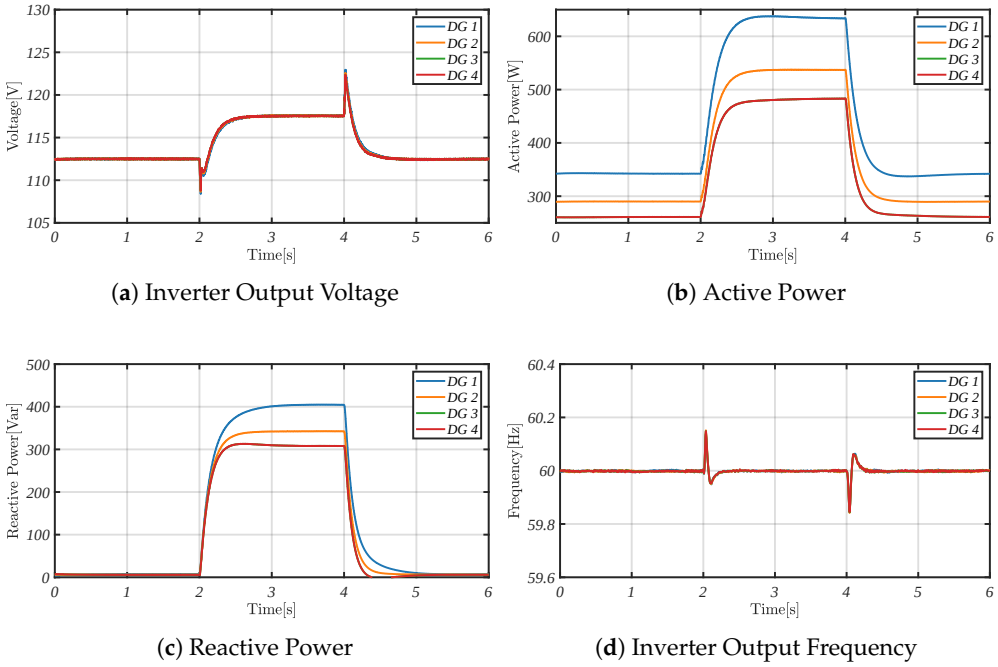

(**a**) Inverter Output Voltage (**b**) Active Power

(**c**) Reactive Power (**d**) Inverter Output Frequency

Figure 26. Simulation results of four DGs with mixed wire using proposed droop control.

Simulation results under inductive and mixed line impedance conditions demonstrate a significant reduction in harmonic distortion for both current and voltage waveforms. Specifically, the ANNDC method achieves lower Total Harmonic Distortion (THD) in the current Fast Fourier Transform (FFT) analysis compared to the CDC approach, indicating superior power quality, as shown in Figures 27–30. Under nonlinear load conditions, the ANNDC control method reduces voltage harmonics more effectively, as evidenced by the voltage FFT analysis in Figures 31–34.

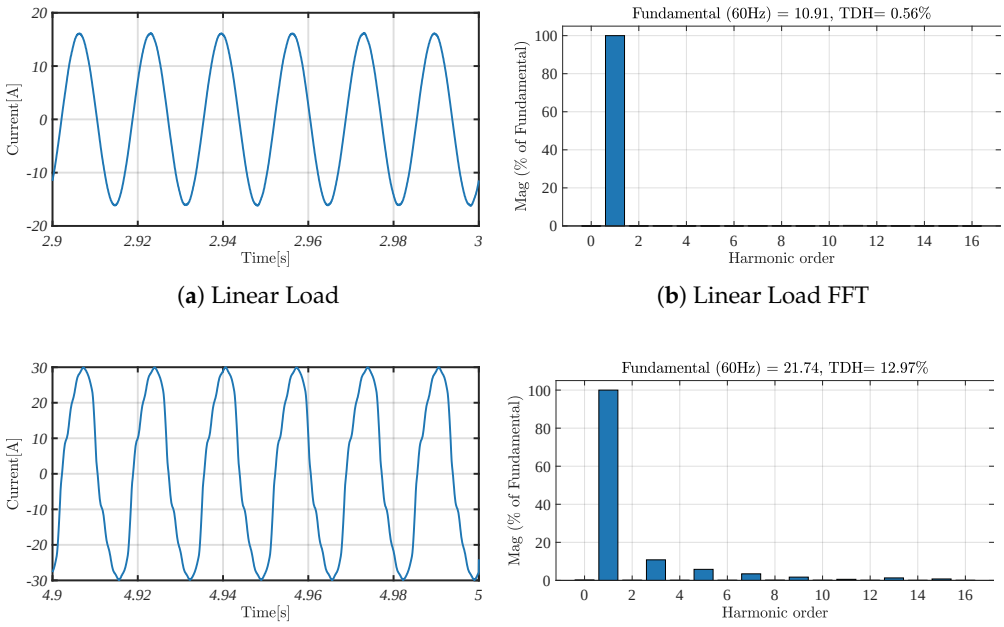

(**a**) Linear Load (**b**) Linear Load FFT

(**c**) Non−Linear Load (**d**) Non-Linear Load FFT

Figure 27. Current FTT for inductive wire for CDC.

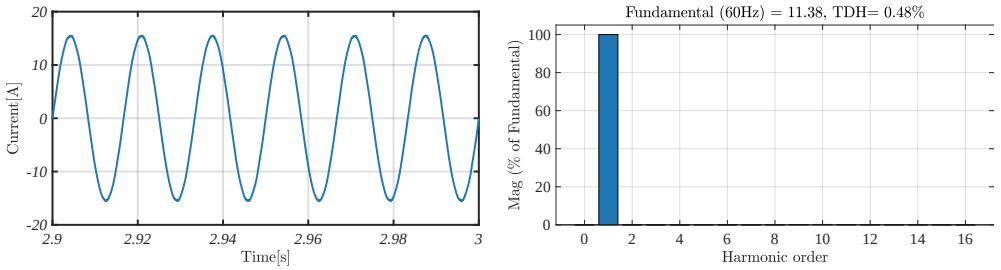

(**a**) Linear Load (**b**) Linear Load FFT

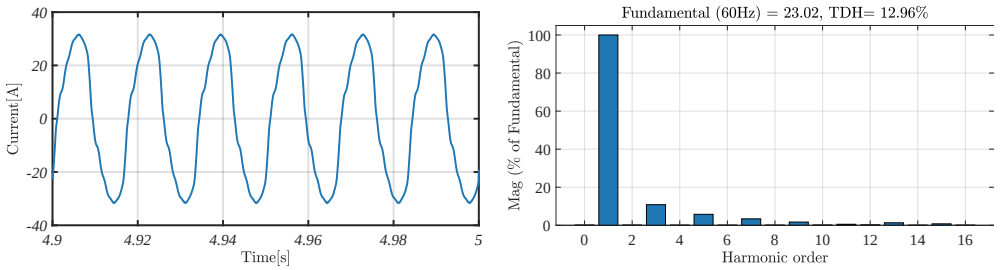

(**c**) Non-Linear Load (**d**) Non-Linear Load FFT

Figure 28. Current FTT for inductive wire for proposed droop control.

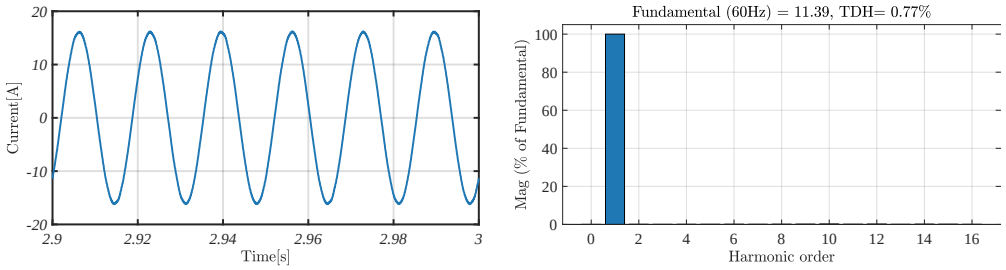

(**a**) Linear Load Only (**b**) Linear Load Only FFT

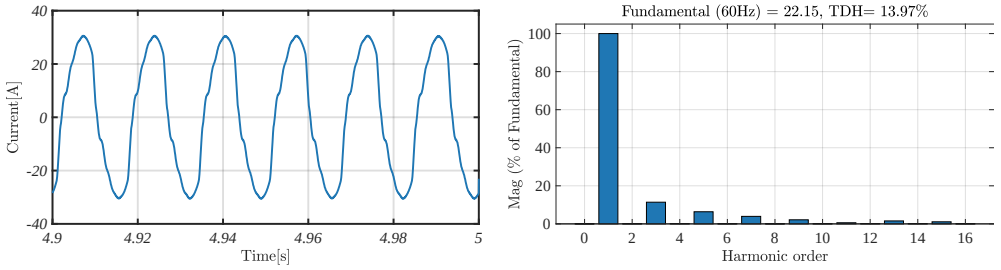

(**c**) Non-Linear + Linear Load (**d**) Non-Linear + Linear Load FFT

Figure 29. Current FTT for mixed wire for CDC.

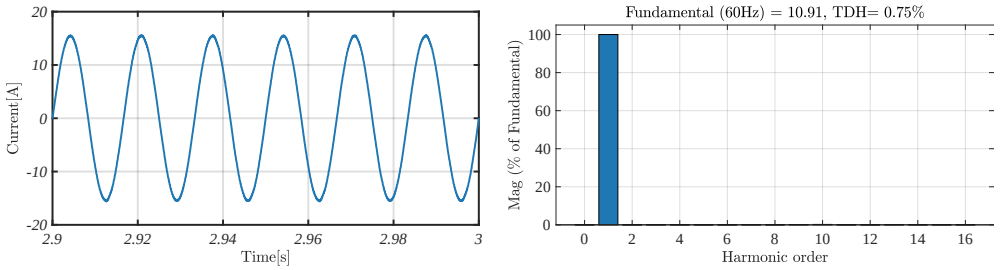

(**a**) Linear Load Only (**b**) Linear Load Only FFT

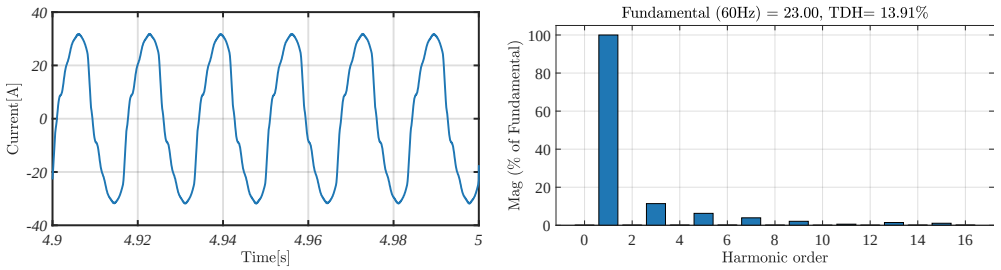

(**c**) Non-Linear + Linear Load (**d**) Non-Linear + Linear Load FFT

Figure 30. Current FTT for mixed wire for CDC.

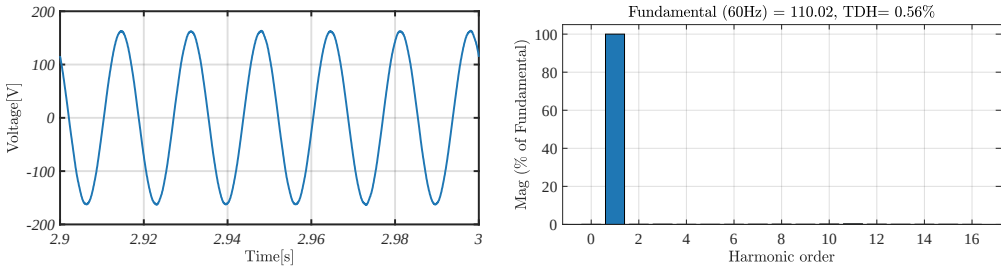

(**a**) Linear Load Only (**b**) Linear Load Only FFT

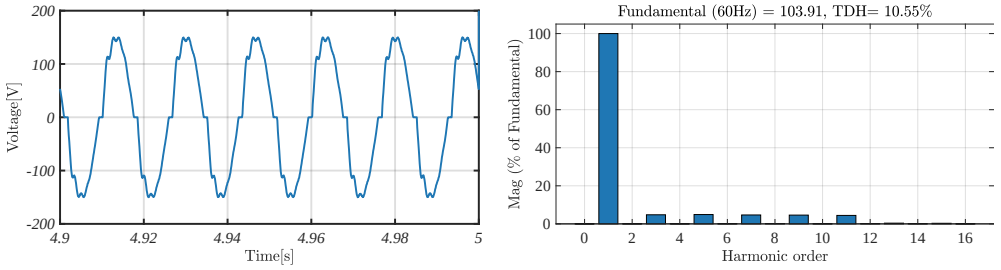

(**c**) Non-Linear + Linear Load (**d**) Non-Linear + Linear Load FFT

Figure 31. Voltage FTT for inductive wire for CDC.

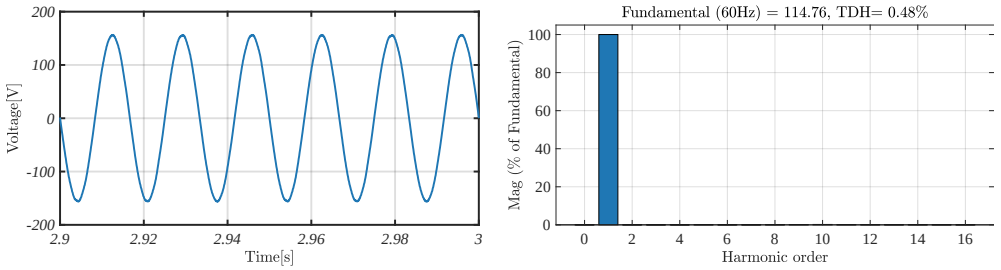

(**a**) Linear Load Only (**b**) Linear Load Only FFT

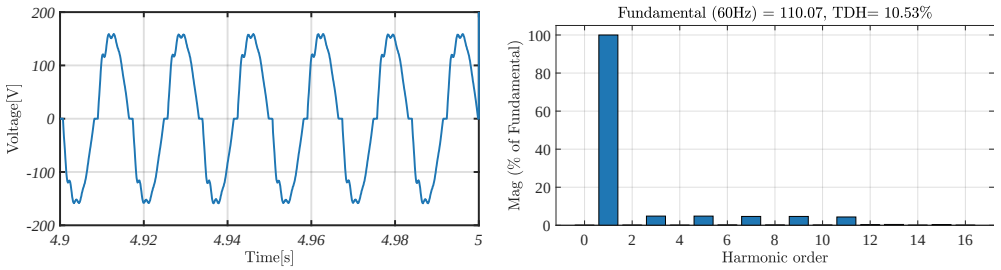

(**c**) Non-Linear + Linear Load (**d**) Non-Linear + Linear Load FFT

Figure 32. Voltage FTT for inductive wire for proposed droop control.

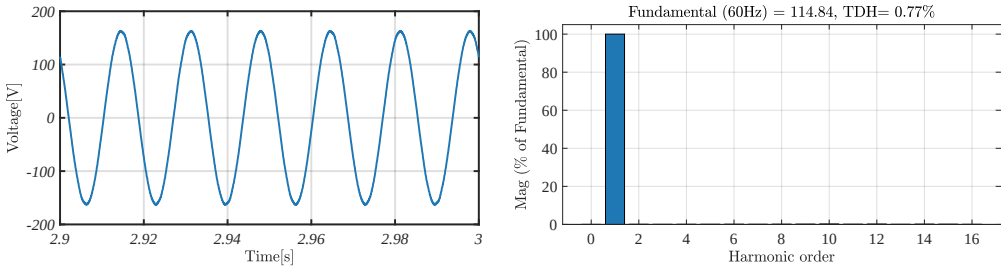

(**a**) Linear Load (**b**) Linear Load FFT

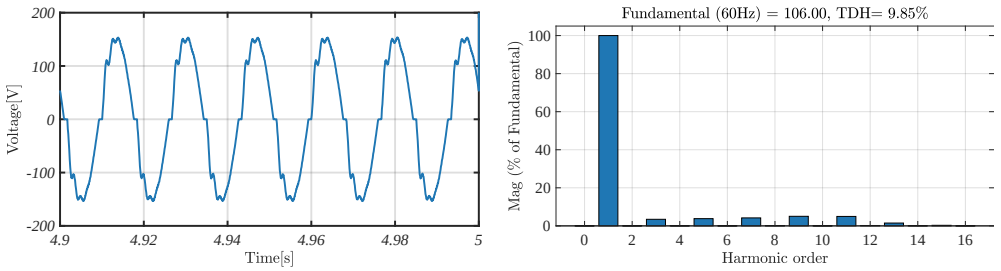

(**c**) Non-Linear Load (**d**) Non-Linear Load FFT

Figure 33. Voltage FTT for mixed wire for CDC.

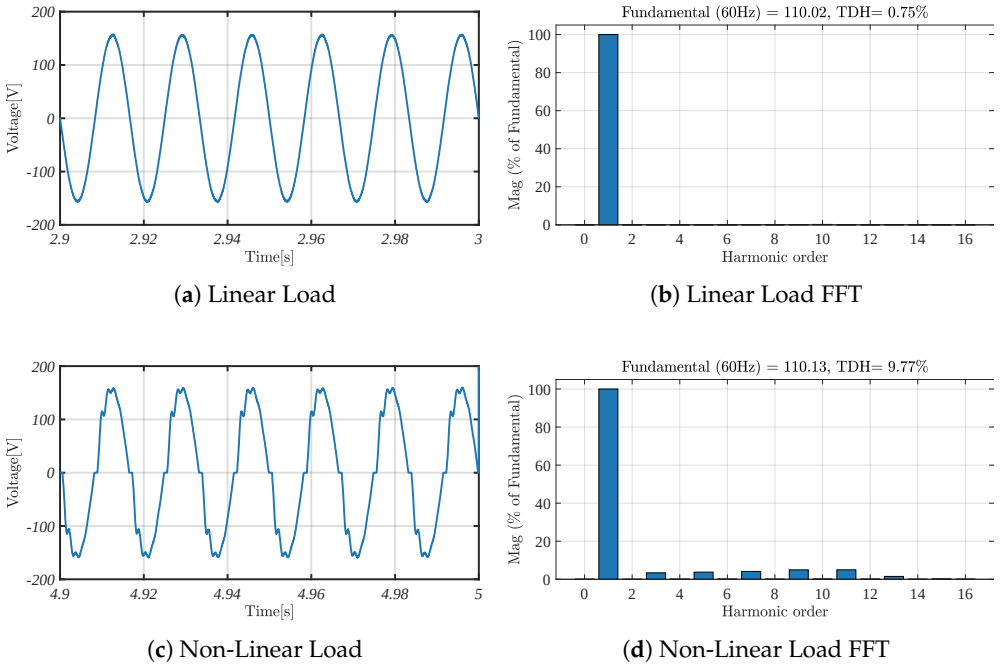

(**a**) Linear Load (**b**) Linear Load FFT

(**c**) Non-Linear Load (**d**) Non-Linear Load FFT

Figure 34. Voltage FTT for mixed wire for proposed droop control.

Tables 4 and 5 summarize the THD results, providing a quantitative comparison of the ANNDC and CDC methods under different line and load conditions in the mesh grid structure. The analysis focuses on both current and voltage THD values, fundamental amplitudes, and the effects of linear and nonlinear loads.

Under linear load conditions, both control methods exhibit low THD values for current and voltage, indicating effective harmonic suppression. However, the ANNDC method consistently achieves slightly lower THD values compared with the CDC method. For instance, in the inductive line scenario, the ANNDC reduces the current THD from 0.56% to 0.48% and the voltage THD from 0.56% to 0.48%. Similar improvements are observed in the mixed−line scenario.

With the introduction of nonlinear loads, THD values increase significantly due to the harmonic components generated by the nonlinear elements. Despite this increase, the ANNDC method demonstrates marginally better performance in mitigating harmonics compared with the CDC method. In the inductive line with linear and nonlinear loads, the ANNDC reduces the current THD from 12.97% (CDC) to 12.96% and the voltage THD from 10.55% to 10.53%. Although the differences are slight, they indicate the ANNDC's enhanced capability to handle harmonic distortions.

Moreover, the ANNDC method maintains the fundamental voltage amplitudes closer to the nominal value of 110 V compared with the CDC method, especially under nonlinear load conditions. For example, in the inductive line with linear and nonlinear loads, the ANNDC maintains the voltage at 110.07 V, whereas the CDC method experiences a drop to 103.91 V. This improved voltage regulation is critical for maintaining power quality and protecting sensitive equipment.

In the mixed−line scenario, the ANNDC method also exhibits better performance. The current and voltage THD values are consistently lower than those achieved by the CDC method. By maintaining the voltage closer to the nominal value, the ANNDC method reduces the impact of line impedance variations on the system's performance.

These results highlight the ANNDC method's effectiveness in enhancing power quality by reducing harmonic distortions and maintaining voltage stability. The ability to achieve lower THD values is crucial for MG operations, as it minimizes losses, prevents equipment overheating, and extends the lifespan of electrical components.

Table 4. Summary of current THD results in mesh grid structure.

Line Type	Control	Load Type	Fundamental [A]	THD [%]
Inductive	CDC	Linear	10.91	0.56
		Linear + Nonlinear	21.74	12.97
	ANNDC	Linear	11.38	0.48
		Linear + Nonlinear	23.02	12.96
Mixed	CDC	Linear	10.91	0.77
		Linear + Nonlinear	22.15	13.97
	ANNDC	Linear	11.39	0.75
		Linear + Nonlinear	23.00	13.91

Table 5. Summary of voltage THD results in mesh grid structure.

Line Type	Control	Load Type	Fundamental [V]	THD [%]
Inductive	CDC	Linear	114.76	0.56
		Linear + Nonlinear	103.91	10.55
	ANNDC	Linear	110.02	0.48
		Linear + Nonlinear	110.07	10.53
Mixed	CDC	Linear	114.84	0.77
		Linear + Nonlinear	106.00	9.85
	ANNDC	Linear	110.02	0.75
		Linear + Nonlinear	110.13	9.77

Overall, the findings validate the robustness and adaptability of the proposed control strategy. The ANNDC method consistently outperforms the CDC method across various scenarios, demonstrating its potential to enhance the efficiency of MG operations. Its ability to dynamically adjust to changing operational conditions and deliver improved power quality makes it a viable solution for modern DGs.

6. Conclusions

An ANNDC strategy optimized using PSO was proposed for MG applications. Comprehensive simulations under various operating conditions demonstrated that the ANNDC method significantly enhances MG performance compared with CDC techniques. The key advancements achieved through this approach include the following:

1. **Enhanced voltage stability:** The ANNDC strategy effectively reduced voltage deviations, maintaining an average deviation within 0.5% of the nominal voltage, whereas CDC methods exhibited deviations of up to 6%. This improvement ensures reliable MG operation and protects sensitive equipment from voltage fluctuations.
2. **Improved frequency stability:** The ANNDC method achieved superior frequency regulation, with average deviations of only 0.15 Hz from the nominal 60 Hz frequency, outperforming CDC methods that had deviations of up to 0.4 Hz. Enhanced frequency stability is crucial for consistent MG performance under dynamic load conditions.
3. **Accurate power sharing:** The ANNDC approach delivered substantial improvements in power−sharing accuracy among DG units, achieving errors below 0.5% compared with errors of up to 7% with CDC methods. Precise power sharing maintains balanced load distribution and prevents overloading of individual units.
4. **Robustness to nonlinear loads:** The proposed method effectively managed nonlinear loads, maintaining THD levels within acceptable limits. The ANNDC method achieved lower THD values in both current and voltage waveforms compared with the CDC method, enhancing power quality in MGs with diverse load types.
5. **Real−time adaptability:** leveraging the integration of ANN and PSO, the ANNDC method enables real−time adjustment of control parameters, providing robust and

adaptive responses to changing MG environments, including variations in load demand, network topology, and line impedances.

These results demonstrate the potential of integrating ANN and PSO in droop control strategies to develop more efficient, stable, and adaptable solutions for modern power systems. The ANNDC method enhances MG reliability, power quality, and scalability, making it suitable for practical implementation in complex MG configurations.

Future work will focus on the real−world implementation and experimental validation of the proposed ANNDC method. This includes deploying the strategy in actual MG setups to assess its performance under practical constraints and operational challenges. Additionally, evaluating the scalability of the method in larger MG configurations with a higher number of DG units and integrating renewable energy sources will be explored. Investigating the method's performance under fault conditions such as short circuits or sudden disconnections and its compatibility with other advanced control strategies, like model predictive control or distributed optimization algorithms, could further enhance its applicability.

In conclusion, this work lays a solid foundation for advancing MG control strategies and promoting the adoption of sustainable and decentralized energy systems. By effectively addressing challenges related to voltage and frequency stability, power−sharing accuracy, and adaptability, the ANNDC method contributes to the development of resilient and efficient MGs. Implementing such advanced control strategies supports the transition towards smarter and more sustainable power grids, capable of meeting the evolving demands of modern society.

Author Contributions: Conceptualization, S.B. and H.F.-B.; methodology, S.B.; software, S.B.; validation, S.B. and H.F.-B.; formal analysis, S.B.; investigation, S.B.; resources, H.F.-B.; data curation, S.B.; writing—original draft preparation, S.B.; writing—review and editing, S.B. and H.F.-B.; visualization, S.B.; supervision, H.F.-B.; project administration, H.F.-B.; funding acquisition, H.F.-B. All authors have read and agreed to the published version of the manuscript.

Funding: This research received no external funding.

Data Availability Statement: Data is available upon request, subject to privacy restrictions.

Acknowledgments: This work was financially supported by the École de technologie supérieure-ÉTS Montréal, Research and Development Fund, Canada.

Conflicts of Interest: The authors declare no conflicts of interest.

References

1. Mehta, S.; Basak, P. A comprehensive review on control techniques for stability improvement in microgrids. *Int. Trans. Electr. Energy Syst.* **2021**, *31*, e12822. [CrossRef]
2. Espina, E.; Llanos, J.; Burgos-Mellado, C.; Cárdenas-Dobson, R.; Martínez-Gómez, M.; Sáez, D. Distributed Control Strategies for Microgrids: An Overview. *IEEE Access* **2020**, *8*, 193412–193448. [CrossRef]
3. Bouzid, A.M.; Guerrero, J.M.; Cheriti, A.; Bouhamida, M.; Sicard, P.; Benghanem, M. A survey on control of electric power distributed generation systems for microgrid applications. *Renew. Sustain. Energy Rev.* **2015**, *44*, 751–766. [CrossRef]
4. Bevrani, H.; Francois, B.; Ise, T. *Microgrid Dynamics and Control*; John Wiley and Sons, Inc.: Hoboken, NJ, USA, 2017.
5. Han, Y.; Li, H.; Shen, P.; Coelho, E.A.A.; Guerrero, J.M. Review of Active and Reactive Power Sharing Strategies in Hierarchical Controlled Microgrids. *IEEE Trans. Power Electron.* **2017**, *32*, 2427–2451. [CrossRef]
6. Han, H.; Hou, X.; Yang, J.; Wu, J.; Su, M.; Guerrero, J.M. Review of Power Sharing Control Strategies for Islanding Operation of AC Microgrids. *IEEE Trans. Smart Grid* **2016**, *7*, 200–215. [CrossRef]
7. Lu, L.Y.; Chu, C.C. Consensus-Based Droop Control of Isolated Micro-Grids by ADMM Implementations. *IEEE Trans. Smart Grid* **2018**, *9*, 5101–5112. [CrossRef]
8. Hoa Thi Pham, X. Power sharing strategy in islanded microgrids using improved droop control. *Electr. Power Syst. Res.* **2020**, *180*, 106164. [CrossRef]
9. Lu, L.Y.; Chu, C.C. Consensus-Based Secondary Frequency and Voltage Droop Control of Virtual Synchronous Generators for Isolated AC Micro-Grids. *IEEE J. Emerg. Sel. Top. Circuits Syst.* **2015**, *5*, 443–455. [CrossRef]
10. Mestriner, D.; Labella, A.; Brignone, M.; Bonfiglio, A.; Procopio, R. A transient stability approach for the analysis of droop-controlled islanded microgrids. *Electr. Power Syst. Res.* **2020**, *187*, 106509. [CrossRef]

11. Lin, S.W.; Chu, C.C.; Tung, C.F. Data-Driven Distributed Q-Learning Droop Control for Frequency Synchronization and Voltage Restoration in Isolated AC Micro-Grids. *IEEE Trans. Ind. Appl.* **2023**, *59*, 7306–7317. [CrossRef]
12. Liu, B.; Song, Z.; Yu, B.; Yang, G.; Liu, J. A Feedforward Control-Based Power Decoupling Strategy for Grid-Forming Grid-Connected Inverters. *Energies* **2024**, *17*, 424. [CrossRef]
13. Wang, C.; Jiao, S.; Zhang, Y.; Wang, X.; Li, Y. Adaptive Variable Universe Fuzzy Droop Control Based on a Novel Multi-Strategy Harris Hawk Optimization Algorithm for a Direct Current Microgrid with Hybrid Energy Storage. *Energies* **2024**, *17*, 5296. [CrossRef]
14. Ding, M.; Tao, Z.; Hu, B.; Tan, S.; Yokoyama, R. Parallel Operation Strategy of Inverters Based on an Improved Adaptive Droop Control and Equivalent Input Disturbance Approach. *Electronics* **2024**, *13*, 486. [CrossRef]
15. Lasabi, O.; Swanson, A.; Jarvis, L.; Aluko, A.; Goudarzi, A. Coordinated Hybrid Approach Based on Firefly Algorithm and Particle Swarm Optimization for Distributed Secondary Control and Stability Analysis of Direct Current Microgrids. *Sustainability* **2024**, *16*, 1204. [CrossRef]
16. Zhang, W.; Wang, Y.; Han, F.; Yang, R. Composite Sliding Mode Control of Phase Circulating Current for the Parallel Three-Phase Inverter Systems. *Energies* **2024**, *17*, 1389. [CrossRef]
17. Chu, Y.; Fei, J.; Hou, S. Adaptive Global Sliding-Mode Control for Dynamic Systems Using Double Hidden Layer Recurrent Neural Network Structure. *IEEE Trans. Neural Netw. Learn. Syst.* **2020**, *31*, 1297–1309. [CrossRef]
18. Kong, W.; Dong, Z.Y.; Jia, Y.; Hill, D.J.; Xu, Y.; Zhang, Y. Short-Term Residential Load Forecasting Based on LSTM Recurrent Neural Network. *IEEE Trans. Smart Grid* **2019**, *10*, 841–851. [CrossRef]
19. Lin, F.J.; Chen, C.I.; Xiao, G.D.; Chen, P.R. Voltage Stabilization Control for Microgrid With Asymmetric Membership Function-Based Wavelet Petri Fuzzy Neural Network. *IEEE Trans. Smart Grid* **2021**, *12*, 3731–3741. [CrossRef]
20. Li, D.; Liu, P.; Zhang, Z.; Zhang, L.; Deng, J.; Wang, Z.; Dorrell, D.G.; Li, W.; Sauer, D.U. Battery Thermal Runaway Fault Prognosis in Electric Vehicles Based on Abnormal Heat Generation and Deep Learning Algorithms. *IEEE Trans. Power Electron.* **2022**, *37*, 8513–8525. [CrossRef]
21. Li, D.; Zhang, Z.; Liu, P.; Wang, Z.; Zhang, L. Battery Fault Diagnosis for Electric Vehicles Based on Voltage Abnormality by Combining the Long Short-Term Memory Neural Network and the Equivalent Circuit Model. *IEEE Trans. Power Electron.* **2021**, *36*, 1303–1315. [CrossRef]
22. Llerena-Pizarro, O.; Proenza-Perez, N.; Tuna, C.E.; Silveira, J.L. A PSO-BPSO Technique for Hybrid Power Generation System Sizing. *IEEE Lat. Am. Trans.* **2020**, *18*, 1362–1370. [CrossRef]
23. Zouari, M.; Baklouti, N.; Sanchez-Medina, J.; Kammoun, H.M.; Ayed, M.B.; Alimi, A.M. PSO-Based Adaptive Hierarchical Interval Type-2 Fuzzy Knowledge Representation System (PSO-AHIT2FKRS) for Travel Route Guidance. *IEEE Trans. Intell. Transp. Syst.* **2022**, *23*, 804–818. [CrossRef]
24. Rodrigues, F.; Molina, Y.; Araujo, C. Simultaneous Tuning of AVR and PSS Using Particle Swarm Optimization with Two Stages. *IEEE Lat. Am. Trans.* **2020**, *18*, 1623–1630. [CrossRef]
25. El Moubarek Bouzid, A.; Sicard, P.; Yamane, A.; Paquin, J.N. Simulation of droop control strategy for parallel inverters in autonomous AC microgrids. In Proceedings of the 2016 8th International Conference on Modelling, Identification and Control (ICMIC), Algiers, Algeria, 15–17 November 2016; pp. 701–706. [CrossRef]
26. Fan, B.; Li, Q.; Wang, W.; Yao, G.; Ma, H.; Zeng, X.; Guerrero, J.M. A Novel Droop Control Strategy of Reactive Power Sharing Based on Adaptive Virtual Impedance in Microgrids. *IEEE Trans. Ind. Electron.* **2022**, *69*, 11335–11347. [CrossRef]
27. Triki, Y.; Bechouche, A.; Seddiki, H.; Abdeslam, D.O. Improved D-Q Frame Controller for Stand-Alone Single-Phase Inverters. In Proceedings of the 2020 IEEE International Conference on Industrial Technology (ICIT), Buenos Aires, Argentina, 26–28 February 2020. [CrossRef]
28. Bisht, R.; Subramaniam, S.; Bhattarai, R.; Kamalasadan, S. Adaptive Minimum Variance Control of Grid Connected Single Phase Inverters in Synchronously Rotating DQ Reference Frame. In Proceedings of the 2018 IEEE Industry Applications Society Annual Meeting (IAS), Portland, OR, USA, 23–27 September 2018. [CrossRef]
29. Xu, J.; Qian, H.; Hu, Y.; Bian, S.; Xie, S. Overview of SOGI-Based Single-Phase Phase-Locked Loops for Grid Synchronization Under Complex Grid Conditions. *IEEE Access* **2021**, *9*, 39275–39291. [CrossRef]
30. Khenar, M.; Taheri, S.; Cretu, A.M.; Hosseini, S.; Pouresmaeil, E. PSO-Based Modeling and Analysis of Electrical Characteristics of Photovoltaic Module Under Nonuniform Snow Patterns. *IEEE Access* **2020**, *8*, 197484–197498. [CrossRef]